ANALYSIS AND IMPLEMENTATION OF SPATIAL FILTERS IN THE QUASI-STATIC REGIME WITH APPLICATIONS TO WIRELESS POWER TRANSFER

by

Erik Saturnino Gámez Rodríguez

A dissertation submitted to the faculty of
The University of Utah
in partial fulfillment of the requirements for the degree of

Doctor of Philosophy

Department of Electrical and Computer Engineering

The University of Utah

December 2017

The University of Utah Graduate School

STATEMENT OF DISSERTATION APPROVAL

The dissertation of **Erik Saturnino Gámez Rodríguez**
has been approved by the following supervisory committee members:

Gianluca Lazzi ,	Chair	**July 26 2017** Date Approved
Behrouz Farhang ,	Member	**July 26 2017** Date Approved
Cynthia Furse ,	Member	**July 26 2017** Date Approved
David Schurig ,	Member	**July 26 2017** Date Approved
Douglas A. Christensen ,	Member	**July 26 2017** Date Approved

by **Gianluca Lazzi** , Chair/Dean of
the Department/College/School of **Electrical and Computer Engineering**
and by **David B. Kieda** , Dean of The Graduate School.

ABSTRACT

More than a century ago, in his labs in Colorado Springs and New York, Nikola Tesla started experimenting with wireless power transfer (WPT). His ideas were ahead of his time, but they fell into obscurity shortly after his death. Nowadays, WPT is no longer thought of as science fiction: neural prostheses, wearables, cellphones, and even electric vehicles can be powered through WPT.

In its most common implementation, WPT leverages the magnetic coupling between resonant transmitter and receiver coils to exchange energy. Considerable work is devoted to the design and optimization of WPT antennas; efficiently transmitting the required amount of power can only be accomplished when the coil coupling is in the right range.

In this work, we explore the use of spatial filters in WPT systems. Spatial filters are capable of controlling the harmonic content of an incident wave: subwavelength focal spots, perfect lensing, and diffractionless beams are some of their uses. In the first part of this dissertation, the focus is on the analysis and design of a compact negative permeability metamaterial slab. Compared to other works in the literature, this slab is an extremely small fraction of the wavelength, and works at a low operating frequency. Analysis and experimental validation demonstrate that the resulting metamaterial sample can be used in a 2-coil WPT system to achieve large range and efficiency enhancements.

In the second part of this dissertation, the analysis and implementation of holographic screens is presented. A method to reduce the fabrication complexity of the desired holographic screen while maintaining the fidelity of the prescribed field distribution is presented. We demonstrate our method through the analysis, design, and experimental validation of a nondiffractive beam launcher with a Bessel field distribution. Finally, we utilize the analysis and methods presented in this work to design an antenna capable of prescribing a uniform field distribution. Because of this property, this WPT antenna is capable of transmitting near constant power with near constant efficiency to the target receiver load, without the need of an adaptive compensation system.

For my parents, Saturnino and Rosa Angélica.

CONTENTS

ABSTRACT . . . . . **iii**

LIST OF FIGURES . . . . . **vii**

LIST OF TABLES . . . . . **ix**

ACKNOWLEDGMENTS . . . . . **x**

CHAPTERS

1. INTRODUCTION **1**

1.1 Abstract 1
1.2 Wireless Power Transfer Theory 1
1.3 Significance of Work 3
1.4 References 8

2. COMPACT, LOW-FREQUENCY METAMATERIAL DESIGN FOR WIRELESS POWER TRANSFER EFFICIENCY ENHANCEMENT **10**

2.1 Abstract 10
2.2 Introduction 11
2.3 Background 12
2.3.1 Inductive Wireless Power Transfer 12
2.3.2 Indefinite Metamaterial 14
2.3.3 A Case for Efficiency Enhancement 16
2.4 Design, Fabrication, and Characterization 16
2.4.1 Unit Cell Design 16
2.4.2 Metamaterial Fabrication 18
2.4.3 Metamaterial Validation and Property Extraction 19
2.4.4 Validation of Extracted Properties 21
2.4.5 Effect of Receiver Size 22
2.5 Results 23
2.5.1 Single Turn System Enhancement 24
2.5.2 Multiturn System Enhancement 25
2.6 Conclusions 26
2.7 References 38

3. ON THE GENERATION OF NONDIFFRACTING BEAMS IN EXTREMELY SUBWAVELENGTH APPLICATIONS **41**

3.1 Abstract 41
3.2 Introduction 42
3.3 Methods 43
3.3.1 Analysis Through Harmonic Decomposition 43

3.3.2 Orthogonal Matching Pursuit Implementation 46
3.3.3 Single Port Implementation 47
3.4 Analysis, Design, and Implementation 48
3.4.1 Holographic Screen Design 49
3.4.2 Holographic Screen Fabrication 51
3.5 Results 52
3.5.1 Field Measurements 52
3.5.2 Reduced Decay Design 54
3.6 Conclusions 55
3.7 Acknowledgments 56
3.8 References 68

4. ON THE APPLICATIONS AND INTEGRATION OF SPATIAL FILTERS IN WIRELESS POWER TRANSFER SYSTEMS 71

4.1 Abstract 71
4.2 Introduction 72
4.3 Background 73
4.4 Spatial Filter Design 75
4.5 Results 79
4.6 Conclusions 80
4.7 References 90

5. CONCLUSIONS 93

5.1 Summary of Results 93
5.2 Future Work 95

LIST OF FIGURES

1.1 Circuit schematic of conventional WPT systems. Two coil antennas, L_{TX} and L_{RX} transfer energy through inductive coupling L_M. 6

1.2 Different tradeoffs between link efficiency η_{link} and delivered power P_d can be obtained by modifying the product $k\sqrt{Q_{TX}Q_{LRX}}$. Efficiency and delivered power have been scaled to a maximum of 1 for illustrative purposes. 6

1.3 Mutual inductance dependence on separation between coils for two identical circular single turn coils. Mutual inductance L_M has been normalized in terms of L, the inductance of one single turn coil. Coil to coil separation d is normalized in terms of the radius of the single turn coils r. 7

2.1 2-Coil coupling schematic and circuit equivalent. a) Setup diagram, b) 2-port circuit equivalent. 27

2.2 2-coil WPT system circuit diagram. 27

2.3 Efficiency measurement setup. a) Efficiency measurement setup using metamaterial design, b) efficiency measurement setup in air. 28

2.4 Unit cell diagram and setting for effective property vs. cell spacing study. a) Proposed unit cell, b) setting used for effective property vs. cell spacing study. 29

2.5 Simulated unit cell Q factor vs. number of turns. The simulated ferrite rod had 2 cm in length, 2.5 mm in diameter and a bulk relative permeability of μ_r' = 133. 29

2.6 Simulated properties of ideal metamaterial vs. unit cell spacing. Unit cell parameters are shown in Table 2.1. 30

2.7 Fabricated metamaterial. a) Side view, b) Perspective view. 30

2.8 Metamaterial effect on mutual impedance of 2-coil system. a) Mutual impedance measuring setup, b) measured mutual impedance between 2 coils that are 4 cm apart. 31

2.9 Effective material properties of the fabricated metamaterial sample. 32

2.10 Mutual impedance magnitude measurement vs. simulation. 32

2.11 Receiver radius effect on mutual impedance enhancement. 33

2.12 Mutual impedance magnitude vs. metamaterial sample position. 33

2.13 WPT efficiency measured as a function of coil to coil separation. 34

2.14 Multiturn system efficiency. a) Measurement setup, b) measured and simulated efficiencies. 35

3.1 Depiction of the proposed system. 57

3.2 Holographic screen optimization procedure. 57
3.3 Desired Gaussian tapered Bessel distribution of the $\hat{z}$ component of the magnetic field. a) Field distribution and harmonic composition at focal plane, b) cross-section through a plane passing through the diameter of the coil of the normalized forward propagated field. 58
3.4 Estimation error between desired field distribution and field produced by the holographic screens against number of elements. 59
3.5 Computed distributions and harmonic content for the $\hat{z}$ component of the magnetic field at the focal plane for a 6-element holographic screen. 59
3.6 Fabricated holographic screen. a) Front, b) back 60
3.7 a) Measurement setup, b) measurement probe and holographic screen, c) measurement probe. 61
3.8 Field correlation between measured and desired fields at focal plane versus frequency. 61
3.9 $\hat{z}$ component of the measured magnetic fields. a) normalized field, b) field correlation between measured and desired fields against distance from aperture. 62
3.10 Desired Gaussian tapered field distribution of the $\hat{z}$ component of the magnetic field for the reduced decay beam. a) Desired distribution and harmonic content at focal plane, b) normalized forward propagated field. 63
3.11 Reduced decay holographic screen. a) Front, b) back 64
3.12 Reduced decay holographic screen. Measured to desired field correlation at focal plane versus frequency. 64
3.13 Reduced decay holographic screen. a) Measured $\hat{z}$ component of the magnetic field against distance from the holographic screen, b) field correlation between desired and measured field against distance from the holographic screen. 65
4.1 Standard wireless power transfer system. 81
4.2 Wireless Power Consortium Qi standard coils geometry and performance. . . . 81
4.3 Candidate field distributions and their harmonic spectrum. 82
4.4 Holographic screen optimization flowchart. 83
4.5 Field distribution and correlation error for potential implementations of the desired holographic screen. 84
4.6 Chosen solution against actual implementation. 85
4.7 Field distribution correlation at focal plane against frequency. 86
4.8 Efficiency and power delivery for optimized WPT antenna. 86

LIST OF TABLES

2.1 Unit cell parameters. 36
2.2 Single turn WPT system parameters. 36
2.3 Multiturn WPT system parameters. 37
3.2 Parameters for candidate holographic screens 66
3.3 Multiturn holographic screen implementation parameters 66
3.4 Reduced decay multiturn holographic screen implementation parameters 66
3.1 Solutions to Maxwell equations inside a cylindrical waveguide. 67
4.1 Summary of features outlined in the Wireless Power Consortium Qi standard. 86
4.2 Wireless Power Consortium Qi Standard coil parameters. 87
4.3 Candidate field distributions parameters. 87
4.4 Holographic screen parameters used to generate Figure 4.5a 88
4.5 Refined and final holographic screen parameters. 88
4.6 Single driven port holographic screen loading capacitors and excitation voltages. 89

ACKNOWLEDGMENTS

First of all, I would like to thank my parents: Saturnino Gámez and Rosa Angélica Rodríguez de Gámez, my brothers Carlos and Jonathan, and my family here in Utah and back in El Salvador. Their encouragement and support has been crucial over this decade-long journey.

Secondly, I would like to thank my adviser and friend Gianluca Lazzi. Professor Lazzi has not only provided great advice and years of technical expertise, but has also showed a remarkable level of patience and helped me overcome the many challenges and anxieties that were encountered over the years.

Thirdly, I would like to thank the many friends and colleagues who have accompanied me throughout the years. In particular my current and previous labmates at professor Lazzi's group, with whom I have grown professionally and as a person.

CHAPTER 1

INTRODUCTION

1.1 Abstract

The history of wireless power transfer started long ago when Ampere, Faraday, Maxwell, and many others laid the foundations of electromagnetic theory. One important development that resulted from their work was the realization that power could be transmitted via electromagnetic waves. Pioneers like Nikola Tesla [1,2] helped demonstrate this principle, but it was not until much more recently that the field of wireless power transfer was mature enough for wireless power transfer (WPT) systems to be incorporated into commercial devices. Deep implantation neural stimulators played a big role in the development and popularization of this technology [3,4]. These devices cannot be powered through conventional means, i.e., wires, due to the possibility of medical complications. Neither can the power be harvested from the environment, since the available power is well below most systems requirements [5]. Therefore, a safe and wireless power transfer scheme is required. This chapter presents a brief introduction to the theory and limitations of wireless power transfer, and a brief discussion on the contributions of the present work.

1.2 Wireless Power Transfer Theory

Wireless power transfer (WPT) can be achieved through many different schemes: radiative WPT [1], capacitive WPT [6], inductive WPT [7], etc. Out of these, perhaps the most popular is resonant inductive WPT [3,4,8,9]. In its most common implementation, energy is exchanged via inductive coupling between resonant coils. Most materials have a weak response to the magnetic field; consequently, inductive WPT is preferable in applications where lossy dielectric materials surround the transmitter and receiver antennas, biological tissues in the case of biomedical implants [10–12]. Figure 1.1 shows the circuit schematic for a conventional 2-coil WPT system.

As seen in Figure 1.1, in a conventional WPT system, a power source V_s induces a cur-

rent on the transmitter coil which has inductance L_{TX}. Current is maximized by resonating this coil in series with a capacitor C_{TX}, while losses in the circuit are accounted for in the model by adding a parasitic resistor R_{TX}. Power is then transferred to the receiver, with inductance L_{TX}, through the voltage induced in the receiver coil by the mutual inductance L_M. The receiver coil is resonated through a parallel capacitor C_{RX} to maximize power delivery, and again, losses in elements other than the useful load R_L are accounted for by adding an equivalent resistor R_{RX}. Equations for WPT link efficiency η_{link}, power delivery P_d, and the total impedance seen at the receiver R_{tot} for these systems are derived in [7, 12–16] and repeated here for convenience:

$$\eta_{link} = \frac{k^2 Q_{TX} Q_{LRX}}{1 + k^2 Q_{Tx} Q_{LRX}} \cdot \frac{Q_{LRX}}{QL} \tag{1.1}$$

$$P_d = \frac{V_s^2}{2R_{TX}} \cdot \frac{k^2 Q_{TX} Q_{LRX}}{\left(1 + k^2 Q_{TX} Q_{LRX}\right)^2} \cdot \frac{Q_{LRX}}{QL} \tag{1.2}$$

$$R_{tot} = R_{TX}\left(1 + k^2 Q_{Tx} Q_{RX}\right) \tag{1.3}$$

In these equations, the mutual coupling coefficient is defined as $k = \frac{L_M}{\sqrt{L_{TX} L_{Rx}}}$; the load quality factor as $Q_L = \frac{\omega L_{RX}}{R_L}$; the transmitter quality factor as $Q_{TX} = \frac{\omega L_{TX}}{R_{RX}}$; the receiver quality factor as $Q_{RX} = \frac{R_{RX}}{\omega L_{RX}}$; the loaded receiver quality factor as $Q_{LRX} = \left(Q_L^{-1} + Q_{RX}^{-1}\right)^{-1}$; and V_s is the power supply voltage.

The term $k\sqrt{Q_{TX} Q_{Rx}}$ is common to all of these equations, and can be used to analyze the system in terms of loosely $k\sqrt{Q_{TX} Q_{Rx}} < 1$, strongly $k\sqrt{Q_{TX} Q_{Rx}} > 1$, and critically $k\sqrt{Q_{TX} Q_{Rx}} = 1$ coupled regimes [16]. In the loosely coupled regime, power delivery and efficiency increase with increasing $k\sqrt{Q_{TX} Q_{RX}}$. On the other hand, in the strongly coupled regime efficiency increases with increasing $k\sqrt{Q_{TX} Q_{RX}}$ at the cost of P_d. Maximum P_d for a given source voltage V_s is obtained in the critically coupled regime, but working in this regime fixes efficiency to $\eta_{link} = \frac{1}{2} \cdot \frac{Q_{LRX}}{Q_L}$, which is 50% at most. An inherent tradeoff of

these systems can now be observed: delivering the required amount of power may require a system that works at a suboptimal efficiency. These results are summarized in Figure 1.2.

Efficiently delivering the desired amount of power is further complicated when tolerance and driving circuit limitations are taken into consideration. It is known that, in general, inductive coil coupling decreases as the inverse of the distance between coils cubed, and in some regions faster. Therefore link efficiency, power delivery, and reflected impedance can vary drastically over relative small changes in distance. Matching networks [17] and multicoil [13, 15, 18] systems can be used to reduce the effect of large coupling variations, but their effect is limited due to the large variation in the coupling coefficient k that can result from small changes in distance. As an example, mutual inductance for the case of two parallel and concentric circular single turn coils of radius r separated by a distance d is given by the following formula:

$$L_M = \frac{2\mu_0}{\alpha} r \left[\left(1 - \alpha^2/2\right) K\left(\alpha\right) - E\left(\alpha\right) \right] \tag{1.4}$$

where

$$\alpha = 2\frac{r}{\sqrt{4r^2 + d^2}}$$

μ_0 is the permeability of free space, and $K\left(\alpha\right)$ and $E\left(\alpha\right)$ are the complete elliptical integrals of the second kind. Figure 1.3 shows the ratio of the mutual inductance L_M to the coil self inductance L as a function of the coil-coil separation d divided by the coil radius r.

As expected, Figure 1.3 shows that the mutual inductance L_M, and therefore k, experience an exponential decay as we increase the coil to coil separation d.

1.3 Significance of Work

As discussed in the previous section, designing a WPT system capable of efficiently delivering the required power is challenging and sometimes not possible due to how quickly the mutual coupling k changes with distance. In this work, we explore the use of spatial filters to control the magnetic flux of the transmitter antenna in the proposed WPT systems. It is shown that control over the magnetic flux of the transmitter antenna results

in WPT systems with enhanced range, higher efficiency, and near-constant performance over a designated surface.

Spatial filters can be obtained in a multitude of ways. Nonetheless, this work focuses on two methods: metamaterials and holographic screens. Metamaterials with negative effective properties have been shown to enhance evanescent waves and control the phase of propagating waves [19, 20]. This property can be leveraged in WPT systems, since inductive coupling is basically coupling of evanescent waves. Nonetheless, to be practical, the required metamaterial has to be extremely compact, low loss, and work at low frequencies (less than 10 MHz for most systems). These restrictions are in direct conflict with the requirements for low loss metamaterials, namely, large quality factor unit cells. In this work, we overcame this issue by transitioning from printed circuit unit cells to 3D unit cells. The unit cell used in the proposed metamaterial sample leverages the compact nature and high quality factor of ferrite-loaded solenoids. Analysis and experimental validation are obtained by integrating the metamaterial sample into a 2-coil WPT system. Measurements show that a metamaterial-assisted 2-coil WPT system is capable of doubling the WPT efficiency of the system, or equivalently doubling the range of the original unassisted system.

Not unlike metamaterials, microwave holographic screens have been shown to control the harmonic content of incident waves as well. Nonetheless, to the best of our knowledge, a consistent framework for analyzing their properties and arriving to low-complexity implementations has not been presented in the literature. In this work, we start by analyzing the properties of a holographic screen starting from the prescribed field distribution. It is found that the properties of the beam launched by a holographic screen can be understood through a harmonic decomposition of the target field distribution. Implementation of the desired beam is then achieved through a compressive representation of the original field distribution through the the orthogonal matching pursuit (OMP) algorithm. The analysis and implementation algorithms are then experimentally validated through the fabrication of a nondiffractive beam launcher. A low-complexity holographic screen capable of launching an approximate evanescent Bessel beam is designed and the resulting field distribution measured. Measurements demonstrate that the properties of the launched beam approximate the properties of an ideal Bessel beam to a large extent.

Finally, in this work, the integration of holographic screens in wireless power transfer systems is explored. In particular, we design and analyze the properties of a holographic screen capable of generating a uniform distribution of the $\hat{z}$ component of the magnetic field over a target area. Because of its field distribution, the proposed antenna is capable of delivering near constant power to a receiver at near constant efficiency, as long as the receiver is located inside the area where the $\hat{z}$ component of the magnetic field is prescribed to be constant. This property allows for wireless power transfer systems with reduced complexity and high efficiency.

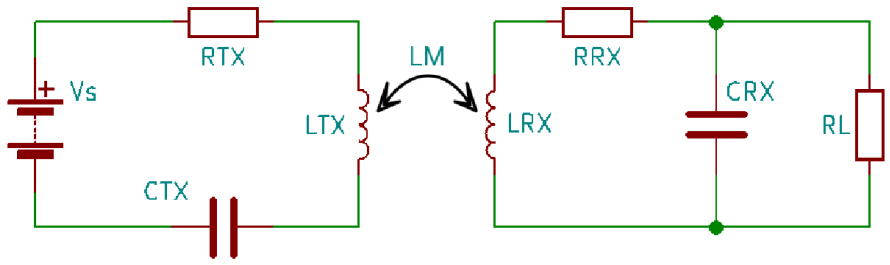

Figure 1.1: Circuit schematic of conventional WPT systems. Two coil antennas, L_{TX} and L_{RX} transfer energy through inductive coupling L_M.

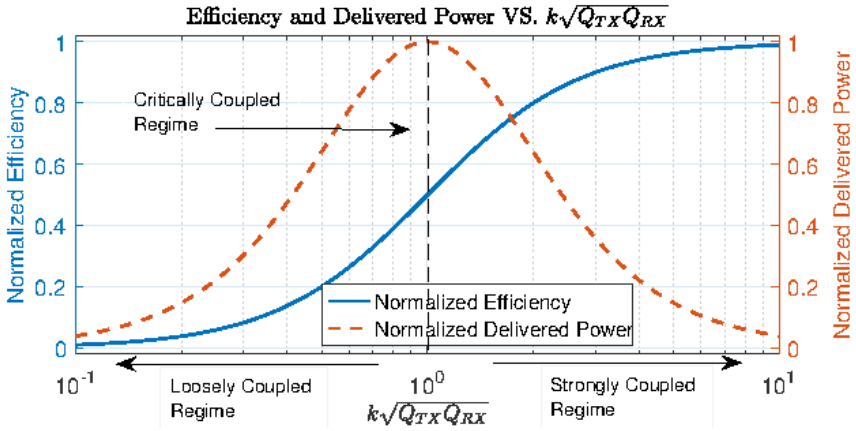

Figure 1.2: Different tradeoffs between link efficiency η_{link} and delivered power P_d can be obtained by modifying the product $k\sqrt{Q_{TX}Q_{LRX}}$. Efficiency and delivered power have been scaled to a maximum of 1 for illustrative purposes.

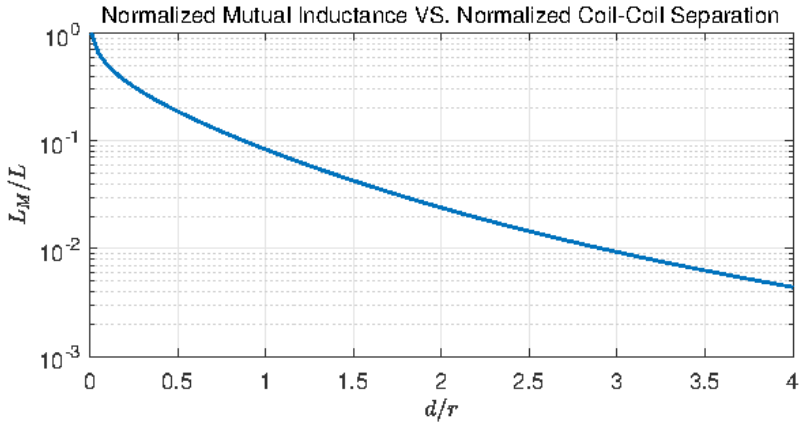

Figure 1.3: Mutual inductance dependence on separation between coils for two identical circular single turn coils. Mutual inductance L_M has been normalized in terms of L, the inductance of one single turn coil. Coil to coil separation d is normalized in terms of the radius of the single turn coils r.

1.4 References

[1] J. Garnica, R. A. Chinga, and J. Lin, "Wireless power transmission: From far field to near field," *Proceedings of the IEEE*, vol. 101, no. 6, pp. 1321–1331, June 2013.

[2] A. S. Marincic, "Nikola Tesla and the wireless transmission of energy," *IEEE Transactions on Power Apparatus and Systems*, vol. PAS-101, no. 10, pp. 4064–4068, Oct 1982.

[3] W. Liu, K. Vichienchom, M. Clements, S. C. DeMarco, C. Hughes, E. McGucken, M. S. Humayun, E. D. Juan, J. D. Weiland, and R. Greenberg, "A neuro-stimulus chip with telemetry unit for retinal prosthetic device," *IEEE Journal of Solid-State Circuits*, vol. 35, no. 10, pp. 1487–1497, Oct 2000.

[4] F. G. Zeng, S. Rebscher, W. Harrison, X. Sun, and H. Feng, "Cochlear implants: System design, integration, and evaluation," *IEEE Reviews in Biomedical Engineering*, vol. 1, pp. 115–142, 2008.

[5] A. Khaligh, P. Zeng, and C. Zheng, "Kinetic energy harvesting using piezoelectric and electromagnetic technologies x2014, state of the art," *IEEE Transactions on Industrial Electronics*, vol. 57, no. 3, pp. 850–860, March 2010.

[6] M. Kline, I. Izyumin, B. Boser, and S. Sanders, "Capacitive power transfer for contactless charging," in *2011 Twenty-Sixth Annual IEEE Applied Power Electronics Conference and Exposition (APEC)*, March 2011, pp. 1398–1404.

[7] G. A. Covic and J. T. Boys, "Inductive power transfer," *Proceedings of the IEEE*, vol. 101, no. 6, pp. 1276–1289, June 2013.

[8] S. Li and C. C. Mi, "Wireless power transfer for electric vehicle applications," *IEEE Journal of Emerging and Selected Topics in Power Electronics*, vol. 3, no. 1, pp. 4–17, March 2015.

[9] J. Kim, J. Kim, S. Kong, H. Kim, I. S. Suh, N. P. Suh, D. H. Cho, J. Kim, and S. Ahn, "Coil design and shielding methods for a magnetic resonant wireless power transfer system," *Proceedings of the IEEE*, vol. 101, no. 6, pp. 1332–1342, June 2013.

[10] G. Lazzi, "Thermal effects of bioimplants," *IEEE Engineering in Medicine and Biology Magazine*, vol. 24, no. 5, pp. 75–81, Sept 2005.

[11] K. Gosalia, J. Weiland, M. Humayun, and G. Lazzi, "Thermal elevation in the human eye and head due to the operation of a retinal prosthesis," *IEEE Transactions on Biomedical Engineering*, vol. 51, no. 8, pp. 1469–1477, Aug 2004.

[12] U. M. Jow and M. Ghovanloo, "Modeling and optimization of printed spiral coils in air, saline, and muscle tissue environments," *IEEE Transactions on Biomedical Circuits and Systems*, vol. 3, no. 5, pp. 339–347, Oct 2009.

[13] A. K. RamRakhyani, S. Mirabbasi, and M. Chiao, "Design and optimization of resonance-based efficient wireless power delivery systems for biomedical implants," *IEEE Transactions on Biomedical Circuits and Systems*, vol. 5, no. 1, pp. 48–63, Feb 2011.

[14] M. Kiani and M. Ghovanloo, "The circuit theory behind coupled-mode magnetic resonance-based wireless power transmission," *IEEE Transactions on Circuits and Systems I: Regular Papers*, vol. 59, no. 9, pp. 2065–2074, Sept 2012.

[15] B. L. Cannon, J. F. Hoburg, D. D. Stancil, and S. C. Goldstein, "Magnetic resonant coupling as a potential means for wireless power transfer to multiple small receivers," *IEEE Transactions on Power Electronics*, vol. 24, no. 7, pp. 1819–1825, July 2009.

[16] A. P. Sample, D. T. Meyer, and J. R. Smith, "Analysis, experimental results, and range adaptation of magnetically coupled resonators for wireless power transfer," *IEEE Transactions on Industrial Electronics*, vol. 58, no. 2, pp. 544–554, Feb 2011.

[17] A. P. Sample, B. H. Waters, S. T. Wisdom, and J. R. Smith, "Enabling seamless wireless power delivery in dynamic environments," *Proceedings of the IEEE*, vol. 101, no. 6, pp. 1343–1358, June 2013.

[18] A. K. RamRakhyani and G. Lazzi, "On the design of efficient multi-coil telemetry system for biomedical implants," *IEEE Transactions on Biomedical Circuits and Systems*, vol. 7, no. 1, pp. 11–23, Feb 2013.

[19] J. Pendry, "Negative refraction makes a perfect lens," *Physical Review Letters*, vol. 85, October 2000.

[20] V. G. Veselago, "The electrodynamics of substances with simultaneously negative values of ϵ and μ," *Sov. Phys. Usp*, vol. 10, 1968.

CHAPTER 2

COMPACT, LOW-FREQUENCY METAMATERIAL DESIGN FOR WIRELESS POWER TRANSFER EFFICIENCY ENHANCEMENT

Metamaterials have been proposed as a way of enhancing inductive wireless power transfer efficiency. Nonetheless, the designs presented in the literature are physically large and work at very high frequencies (10's of MHz and above), making them impractical for use in common applications of wireless power transfer. In this chapter, we present the design and analysis of a metamaterial sample that manages to overcome these issues. This metamaterial sample is fabricated, and the resulting enhancement on the efficiency of the metamaterial-assisted wireless power transfer is measured.

2.1 Abstract

An extremely compact and low frequency metamaterial design is presented in the following work. A ferrite loaded solenoid with a size on the order of 1/10000 of the wavelength of operation is used as the unit cell of the proposed metamaterial. This unit cell allows for the construction of a 77-unit-cell sample with dimensions of 6 cm x 6 cm x 2 cm and operating at a working frequency of 5.57 MHz. Measurements show that the metamaterial-assisted system efficiency is increased to 20% from 10% in the conventional system at a working distance of 4.5 cm. Alternatively, for a target efficiency of 10 %, the range of the system can be extended from 4.5 cm to 8.8 cm by using the proposed metamaterial, a 4.3 cm, or 95 % extension over the original system range. The proposed metamaterial design, characterized by compactness, low frequency of operation, and large efficiency enhancement, is useful in a number of applications, such as biomedical telemetry systems and wireless charging.

2.2 Introduction

Wireless Power Transfer (WPT) is a topic that has gained a great deal of attention in recent years. This surge in interest has been fueled by the quick adoption of: mobile computing devices [1], medical implantable devices [2–5], electric cars [6], etc. The preferred method of WPT used in these applications has been resonant inductive coupling [7–10]. Resonant inductive coupling WPT leverages the magnetic fields produced by resonant coils to transmit power. In practice, the efficiency of these systems is limited by the quality factor of the coils and the mutual coupling between them [7–9]. Mutual coupling decays rapidly as a function of distance between the coils (approximately $1/d^3$), thus limiting the applications where efficient WPT can be achieved to those requiring midrange distances (about twice the diameter of the coils).

Metamaterials have been proposed as a way to increase WPT range [10–20]. Metamaterials are materials with engineered polarizable inclusions. By properly designing these inclusions the electromagnetic properties of the material can be manipulated to achieve effective properties that are not found in traditional media [21–26]. Negative permeability $\mu < 0$, negative permittivity $\epsilon < 0$ and negative refractive index $n < 0$ (simultaneous $\mu < 0$ and $\epsilon < 0$) are among the exotic properties that can be achieved with metamaterials. The enhancement seen in WPT systems using left handed metamaterials has been attributed to the exponential growth of the evanescent waves lying within them [10–13,15–17,19,20,24].

Metamaterial designs proposed in the literature are commonly based on printed resonators (spirals, split-rings, wires, etc.) [10, 12, 14, 16, 18, 20, 27–31]. Arrays of these structures are stacked perpendicularly or parallel to the axis of the system on which control of the effective permeability and permittivity is desired. Nonetheless, even the smallest printed unit cell reported in the literature, with a size of approximately $\lambda/800$ [20, 31], is too large to create a practical size metamaterial sample at the working frequency of conventional WPT systems. Furthermore, the higher parasitic losses seen in miniaturized printed unit cells lead to a reduction of the quality factor, which in turn leads to an increase in effective losses. Alternative unit cell designs have been explored in the literature, but even the smallest unit cell size reported to date (the Swiss Roll with a size of $\lambda/1000$ [32]) does not allow for the creation of a practical size metamaterial at a few MHz, the operation frequency of conventional WPT systems.

Recent studies on the use of metamaterials in WPT systems have shown significant range enhancements over conventional systems. Nonetheless, these systems require samples sizes that are too large [10, 14–17, 19, 25], work at significantly higher frequencies [10, 12–14, 20], and have the possibility of reducing working distance when compared to conventional systems [10–17, 19, 25, 26]. Only modest WPT efficiency enhancements have been reported in experimental setups where the working distance was maintained constant [20, 33]. These disadvantages prevent metamaterials from being used in some applications, such as biotelemetry systems. In biotelemetry systems, the operating frequency needs to remain low in order to minimize power deposition in biological tissue. Additionally, the device needs to be compact, to minimize exposure of the body to the induced electromagnetic fields and increase portability. Finally, the working distance of the device needs to be preserved, since the space between the receiver and the transmitter cannot be accessed, if the receiver has been implanted. To the best of our knowledge, a material capable of addressing all of these requirements simultaneously has not yet been reported.

In this work, we propose a ferrite loaded solenoid (a three-dimensional (3-D) unit cell) to overcome the limitations of current metamaterials. Such a unit cell is promising for the construction of compact, low frequency, and low loss metamaterial samples due to its large quality factor and compact size. Section 2.3 presents the background on wireless power transfer and metamaterials. Section 2.3.1 presents the design, fabrication, and characterization of the proposed metamaterial sample. Section 2.5 presents the system tuning, optimization, efficiency simulations, and measurements. Finally, Section 2.6 presents the conclusions.

2.3 Background

A summary of the state-of-the-art on inductive WPT and indefinite metamaterials is presented in this section.

2.3.1 Inductive Wireless Power Transfer

Inductive WPT systems use mutual inductive coupling to transmit energy. A pair of inductively coupled coils can be connected to a Vector Network Analyzer (VNA), which is

depicted in Figure 2.1a, and their 2-port Z-parameters recorded. These Z-parameters can be used in the equivalent circuit model shown in Figure 2.1b. In this circuit, Z_{11} and Z_{22} are the impedances seen at each port when the remaining port is left open, and Z_M represents the mutual impedance between the two coils. Since no assumptions regarding the nature of Z_M have been made, this model is valid even when an object, such as a metamaterial slab, is placed in between the coils.

Equivalent circuits of the two coupled coils are used to create the complete circuit diagram as seen in Figure 2.2. In this diagram, Z_{tx} is the total transmitter impedance (including the transmitter coil), Z_M is the mutual impedance between the transmitter and receiver coils, Z_{rx} is the total impedance of the receiver (including the receiver coil) minus the useful load R_L.

For a series-series resonant WPT system like the one shown in Figure 2.2, Z_{tx} and Z_{rx} are of the form $Z_i = j\omega L_i + \frac{1}{j\omega C_i} + R_i \quad i = tx, rx$, where L_i is the inductance of the ith coil, C_i is the ith coil resonating capacitor, and R_i is the total parasitic resistance of the sub-circuit. The equivalent Z-parameters of the system can be computed from the circuit shown in Figure 2.2; in particular $Z_{11,eq}$ and $Z_{21,eq}$ are given by:

$$Z_{11,eq} = Z_{tx} - Z_M + Z_M||(-Z_M + Z_{rx} + R_L) \tag{2.1}$$

$$Z_{21,eq} = Z_M \frac{R_L}{Z_{rx} + R_L} \tag{2.2}$$

Based on the work presented in [7], we can derive a formula to compute the WPT efficiency of the system using the system Z-parameters:

$$\eta = \frac{|Z_{21,eq}|^2}{\Re\{Z_{11,eq}\}R_L} \times 100 \quad [\%] \tag{2.3}$$

WPT efficiency of multicoil systems is often written in terms of the quality factors of the transmitter and receiver devices, and the coupling coefficients between them [7,9]. The formulation given in this work was chosen due to its convenience. This formulation allows for the computation of efficiency values for WPT systems from parameters derived from

VNA measurements (S-parameters). Another advantage of this formulation is its explicit dependence on mutual impedances. In later sections, we will compute WPT efficiency from mutual impedance measurements in the presence of the proposed metamaterial slab.

Notice that we have modified the formula presented in [7] by replacing $|Z_{11,eq}|$ with $\Re\{Z_{11,eq}\}$. For the case of a WPT system using metamaterials, it is expected that some power will be stored in the metamaterial near-field, even when the transmitter and receiver coils are self-resonant. Therefore, a complex power would be drawn from the power supply. The reactive power needs to be removed from efficiency calculations since it is not dissipated in the circuit.

Finally, it is common to find a series-parallel topology [3, 7] instead of the series-series topology discussed so far. A series equivalent of an ideal parallel RLC circuit can be found by computing the Thevenin equivalent of a capacitor in parallel to a resistor:

$$Z_s = \frac{R_p^2/Z_p}{1+(R_p/|Z_p|)^2}, \quad R_s = \frac{R_p}{1+(R_p/|Z_p|)^2} \tag{2.4}$$

where Z_p is the impedance of the original parallel capacitor, R_p is the resistance of the original parallel resistor, Z_s is the impedance of the equivalent series capacitor, and R_s is impedance of the equivalent series resistor.

2.3.2 Indefinite Metamaterial

The effective properties of metamaterials depend on the properties of the resonant inclusions that comprise them. The resonance of these inclusions gives rise to effective properties that ideally display a Lorentzian dispersion, as shown in Figure 2.9. The strength of this material resonance is partially determined by the quality factor (Q) of its resonant inclusions. High Q resonant inclusions are desirable, since they can lead to lower losses in the metamaterial, but their fabrication is not always possible due to unit-cell and material size limitations. One such limitation is the homogenization requirement, which dictates that an individual cell should be small compared to the wavelength at the operating frequency for effective medium properties to be valid. Additionally, unit cells cannot be arbitrarily large, since a fine enough sampling of the excitation source is required to observe all the properties of an ideal metamaterial [34]. Furthermore, the overall sample

size cannot be arbitrarily large, since most applications impose a size limit for practical use. As a consequence, compact unit cells (on the order of cm) are preferred, even at frequencies in the MHz range.

Among the unit cell designs reported in literature, split ring and spiral resonators are some of the most popular. Usually, the number of rings or turns has to be increased in order to reduce the operating frequency of these resonators [27–30], which can lead to an increased unit cell size. In many cases, and especially at low frequencies (few MHz), the increase of unit cell size leads to an overall metamaterial size that is impractical for many applications. Capacitive loading [35], broadside coupling [30] and multilayer spirals [31] are some of the techniques used to further reduce the size of unit cells. To the best of our knowledge, the most compact, low-frequency metamaterial unit cell reported in literature was the Swiss Roll [23, 32]. The Swiss Roll achieves a lateral size of $\lambda_0/1000$ at 21.3 MHz.

One important fact that differentiates metamaterials from similar approaches using resonant structures is that they are often used off resonance. For example, it can be demonstrated that ideal metamaterials with negative refractive index n = -1 (simultaneous ϵ_r = -1 and μ_r = -1) support perfect lensing [24]. These properties need to be achieved off resonance, since the effect disappears for large material losses. In WPT efficiency enhancement applications, only control of the effective permeability of the material is needed to cause evanescent wave enhancement in the magnetic field. This happens because resonant inductive WPT systems usually work in the low MHz range, and at the length scale of practical devices, the magnetic and electrical fields are uncoupled. It should also be noted that, for WPT efficiency enhancement, we do not need to match the metamaterial impedance to that of free space, since once again, for practical device sizes, the radiated waves are largely suppressed in the low MHz range. Finally, the ideal permeability for WPT enhancement may vary from μ_r = -1 (the ideal permeability of the perfect lens) since the objective is to maximize the mutual impedance, which may not necessarily require the reconstruction of the transmitter field distribution at the receiver (perfect lensing) [12, 13, 15]. Metamaterial properties that enhance the amplitude of the field would result in efficiency enhancements even if the field of the transmitter is not perfectly reconstructed. In fact, some authors have proposed using properties different from the perfect lensing condition, for metamaterials designs used in wireless power transfer [12, 13, 15, 17, 20, 25, 26, 36].

2.3.3 A Case for Efficiency Enhancement

Depending on the application, it may be important to differentiate between range extension and efficiency enhancement. Figure 2.3 shows how efficiency enhancement differs from the range extension considered by other works in this area [10–19, 25, 26]. If the working distance is to be kept constant, adding the metamaterial sample to the conventional WPT system requires that we increase the distance between the receiver and transmitter coils (Figure 2.3a). In an application that requires a certain working distance, the use of the metamaterial would only make sense if the efficiency is increased even at the increased coil separation, as compared to the original system (Figure 2.3b). An example of such an application is biotelemetry systems. In biotelemetry systems, the receiver coil is implanted and the transmitter device is placed outside of the body. Then, the minimum required working distance is equal to the depth of the implantation.

2.4 Design, Fabrication, and Characterization

In the following, we present the analysis, design, fabrication and characterization of the unit cell and metamaterial sample presented in this work.

2.4.1 Unit Cell Design

Careful thought was given to the design of the unit cell used in this work. Cells based on multisplit ring and planar spiral resonators are not likely to meet the requirements of the applications under consideration, since most resonant inductive WPT systems work in the low MHz range. Even extremely compact unit cells like the Swiss Roll [23,32] (which to the best of our knowledge was the most compact cell found in literature) are not suitable, since the reported length (5 cm), lateral size ($\lambda_0/1000$), and operating frequency (21.4 MHz) are too large to be used in common WPT systems.

Inspired in part by the multilayer spiral unit cell and the Swiss Roll, it was realized that an ideal, compact, low-frequency unit cell would need to efficiently use its depth to avoid a large lateral size. It was found that the ferrite loaded solenoid provides such efficient use. This cell has been previously proposed in [22] to attain a large permeability in the low GHz range, and it was considered as a promising candidate for metamaterial EMI. Due to its structure, this cell possesses several properties that are desirable for the

construction of compact low frequency designs: 1) The solenoidal flux coupling allows for a rapid increase in unit cell inductance as the number of turns in the solenoid is increased; 2) This inductance scaling does not impact lateral size; 3) Loading the unit cell with a ferrite material enhances the inductance of the resonator while adding only relatively small losses, thus increasing the Q of the resonator. Higher Q makes it possible to further reduce the operating frequency or losses in the metamaterial without increasing its footprint.

The ferrite loaded solenoidal unit cell also presents new challenges when compared to other unit cells found in the literature; most of them are associated with the use of the ferrite material. Since ferrite materials show relaxation at higher frequencies, the frequency of operation is constrained by the properties of the particular ferrite material. This relaxation can lead to low Q resonators and high loss metamaterials at higher frequencies. Additionally, due to the finite size of the ferrite rods, the effective permeability of the rod decreases near the ends of the solenoid. As a consequence of this, the inductance of the solenoid does not always grow as the square of the number of turns, as would be expected. It is worth noting that a unit cell consisting of only the solenoidal coil would still provide large reductions on lateral size, and could be considered in cases where the ferrite rod does not provide compelling advantages.

The ferrite loaded solenoidal unit cell is depicted in Figure 2.4a. Figure 2.5 shows the simulated Q for an inductor fabricated using the proposed ferrite loaded solenoid. A ferrite rod of length 20 mm and diameter of 2.5 mm with a bulk relative permeability of $\mu_r' = 133$ was used for the simulation. Simulation results were computed using CST Microwave Studio ^{TM}. The Q factors for 15, 20 and 25 turn solenoids made of 24 AWG single strand copper wire (0.511 mm diameter) with a turn spacing of 0.1 mm were computed.

As seen in Figure 2.5, when the number of turns used in the solenoid increases, the Q of the unit cell decreases. The reason is that as the number of turns in the solenoid is increased, the ferrite core effective permeability decreases, since the ends of the solenoid approach the ends of the ferrite rod. As a consequence, the inductance of the solenoid increases at a slower rate than the parasitic resistance of the solenoid, causing a reduction in Q.

It must be noted that it is possible to further optimize the unit cell presented in this work. For example, the solenoid wire could be replaced by Litz wire, which would cause

an enhancement in Q due to its lower resistance. Another possible optimization would explore the effects of wire gauge. Constructing a more compact solenoid reduces the length of the solenoid for the same number of turns, thus reducing the effects of the finite length of the rod, though resistive losses would likely increase. Finally, instead of using a single layer solenoid, a multilayered helix could be used, thus potentially increasing inductance and parasitic capacitances to the point where the unit cell can be made self-resonant. These optimization techniques were not attempted due to lack of the equipment necessary to fabricate enough of these cells to create a metamaterial sample.

Table 2.1 shows the unit cell parameters chosen for the fabrication of the metamaterial. A compromise in the number of turns of the unit cell was necessary, since the number of turns increased inductance at the expense of Q. A unit cell with 20 turns was chosen as the best compromise between Q and inductance.

2.4.2 Metamaterial Fabrication

The compactness of the unit cell chosen in the previous section allows for the fabrication of a very dense metamaterial sample. The larger the number of unit cells the better the effective material properties describe the sample. Nonetheless, increasing the number of cells in the sample increases fabrication complexity, which may not be desirable. In order to explore the effect of unit cell spacing, an infinite single layer metamaterial with varying unit cell spacing was simulated. The unit cell parameters are given in Table 2.1; the unit cell length was aligned with the $\hat{z}$ axis of the model, $E_t = 0$ and $H_t = 0$ boundary conditions were used for the termination in the $\hat{y}$ and $\hat{z}$ axis, respectively, while the ports were placed at opposite ends along the $\hat{x}$ axis. The effective material properties were extracted with an extraction distance equal to the length of the ferrite core, and for lateral cell sizes of 6, 8 and 10 mm using the method proposed by Smith et al. [37]. The results of this experiment are shown in Figure 2.6.

As shown in Figure 2.6, decreasing the unit cell spacing results in a stronger resonance response and a slight frequency shift. The frequency shift seen on the effective material properties is mainly attributed to the larger resonance strength seen in metamaterials built with closely spaced unit cells, but also to the inter-cell coupling. Because of these results, a dense metamaterial sample was chosen, since that cell spacing does not affect metama-

terial size, and the stronger resonant response would, most likely, increase the efficiency enhancement of the system. Constructing this denser metamaterial sample should not be challenging in an industrial setting, since solenoidal coils are used widely in industry and there is specialized equipment to fabricate them.

The metamaterial sample size was set to 6 cm $\times$ 6 cm $\times$ 2 cm, as a compromise between evanescent wave enhancement and compactness. It has been reported in the literature that, in general, a larger metamaterial (in any direction) leads to larger magnetic field enhancement [11, 15]. The metamaterial sample was designed to be anisotropic; it was fabricated using a single layer of 77 unit cells spaced by 6.6 mm in the lateral direction, with each cell aligned with the $\hat{z}$ axis of the system. Therefore, the effective material permeability shows a Lorentzian dispersion along the $\hat{z}$ axis of the system and the properties of air (μ_r = 1) along the $\hat{x}$ and $\hat{y}$ axis. Figure 2.7 shows the constructed metamaterial. The resonance frequency of each of the unit cells used to fabricate the metamaterial sample was measured, and all were found to fall in the range of 3.35 to 3.50 MHz. The consistency of the unit cell parameters is expected to increase if more specialized equipment were to be used.

2.4.3 Metamaterial Validation and Property Extraction

As mentioned in the introduction, an indefinite metamaterial is expected to increase the efficiency of WPT systems due to the enhancement of the evanescent waves that lie within it. This claim can be tested by measuring the mutual impedance between two coils when the metamaterial is placed in between them. Mutual impedance between two coils is defined as the flux seen at the receiver coil normalized to the transmitter coil current; therefore, the flux enhancement caused by the metamaterial would result in an increase in mutual impedance between the coils.

Two 2 cm radius single turn coils made of 24 AWG solid strand copper wire were used to perform the mutual impedance measurements. The coils were placed 4 cm apart: the mutual impedance between the coils was measured in absence of the metamaterial slab and when the metamaterial slab was placed 5 mm away from the excitation coil. For mutual impedance measurements only, a 40 Ω resistor was added to the coils in series in order to provide a broadband impedance match that would not affect the frequency response of the system. This simple impedance match helps reduce the effect of measurement noise.

Figure 2.8a shows the measurement setup.

Figure 2.8b shows the result of performing the measurements described previously. The results of Figure 2.8b show several features that are directly related to the presence of the metamaterial sample. The large enhancement in mutual impedance seen around 5.574 MHz is particularly notable. Another notable observation is that the mutual impedance is frequency dependent, which is expected since the effective material properties of the sample change with frequency. Additionally, it must be pointed out that the frequency at which the mutual impedance achieves its maximum (5.574 MHz) is different from the unit cell resonant frequency (3.35 to 3.50 MHz), which is expected, since negative permeability is achieved above resonance and results in mutual impedance enhancement. Finally, at the frequency of the largest enhancement (5.574 MHz) the unit cell achieves a lateral size of $\lambda_0/10{,}766$, which makes it, to the best of our knowledge, the most compact unit cell presented in the literature.

It is important to show that the measured mutual impedance enhancement seen in Figure 2.8b is a product of the evanescent wave enhancement caused by the metamaterial sample and not just due to the the ferrite rods used in the fabrication of the unit cells. In order to demonstrate this, we fabricated a 6 cm $\times$ 6 cm $\times$ 2 cm material consisting of 32 unit cells, using only the ferrite cores (no solenoidal resonator), with a lateral spacing of about 1.3 cm. It must be noted that replacing the volume of the metamaterial with a ferrite slab of the same dimensions would likely decrease the mutual impedance since ferrite slabs are commonly used for shielding in many applications. The results of this experiment can be seen in Figure 2.8b. As expected, the ferrite core results in an enhancement in mutual impedance. Nonetheless, this enhancement is significantly smaller than the enhancement seen in presence of the metamaterial sample and does not show the same frequency dependence.

It would be desirable to measure the effective properties of the fabricated metamaterial, but such measurements are challenging due to the low operating frequency. Because of this, we opted to extract the properties of the metamaterial through an optimization routine. The setup in Figure 2.8a was simulated in CST Microwave Studio ^{TM}, but the fabricated metamaterial was replaced with an homogeneous anisotropic slab of the same dimensions as the fabricated metamaterial. The simulated slab had the properties of air

along the $\hat{x}$ and $\hat{y}$ directions, while its permeability was constrained to show a Lorentzian dispersion along the $\hat{z}$ direction, thus modeling the intended anisotropic metamaterial design. The CST Microwave Studio ^{TM} Trust Region Framework optimizer was run to find the resonant frequency and damping coefficient of the Lorentzian dispersion that caused the simulated mutual impedance to better match the measured mutual impedances. The mutual impedance data in the range of 5.4 to 5.7 MHz were used to perform this optimization, in order to avoid the parameter extraction uncertainty that would result from using a single frequency sample. During optimization, emphasis was given to the maximum absolute impedance enhancement value and frequency (5.574 MHz), since this was the frequency where maximum WPT efficiency enhancement was expected to be seen. The extracted effective permeability of the metamaterial along the $\hat{z}$ direction is shown in Figure 2.9, while the simulated mutual impedance is shown in Figure 2.8b. The simulated mutual impedance shows excellent agreement with measurements near its peak value, at 5.574 MHz, while degrading as we move away from it. This results from the relatively narrow frequency range used for the numerical fit and the frequency relaxation of the ferrite core, which was not modeled in our simulation. The effective material permeability that results in the largest mutual impedance is found to be μ_r = -0.61 for the system under consideration.

2.4.4 Validation of Extracted Properties

The value of a simulation model is in its predictive capabilities. We compared simulated and measured mutual impedance values in order to validate our simulation model and extracted properties. For this, we simulated and measured mutual impedance for varying coil separations. The coils separation was swept from 4 to 11 cm, while the metamaterial remained 5 mm away from the excitation coil. The maximum mutual impedance magnitude measurement and simulation results are shown in Figure 2.10. For the cases where no metamaterial was used (air), or the ferrite-only material was used, Figure 2.10 shows the mutual impedance measured at the frequency at which the maximum mutual impedance magnitude was measured in the presence of the metamaterial, 5.574 MHz for all coil separations.

As seen in Figure 2.10, excellent agreement was observed between the simulated and

measured maximum mutual impedance magnitudes. Additionally, it can be seen that the maximum magnitude of the mutual impedance in presence of the metamaterial sample is always larger than the mutual impedance in air, and the mutual impedance when using the ferrite-only material, even as the coils were moved further apart within the measuring range.

Equations aimed at predicting the mutual inductance enhancement and wireless power transfer efficiencies caused by negative permeability metamaterials can be found in the literature [11]. The validity of these equations depends on two main assumptions: 1) The coils in the system can be approximated by ideal magnetic dipoles; 2) The lateral size of the metamaterial sample is large enough to be accurately approximated by an infinite metamaterial slab. None of these assumptions are valid in our system, since the characteristic dimension and separation of all elements were very similar. These equations failed at describing our measurements, which helps confirm the results in [15], where the results predicted by the equations in [11] were compared to simulations of systems with finite size metamaterial slabs and finite size coils, and large discrepancies were found.

2.4.5 Effect of Receiver Size

Because some applications may require smaller receiver coils than that considered in the previous section, we decided to test if the type of enhancements seen for the mutual impedance between our coils would be observed for smaller coils as well. To do this, we used our extracted model and simulated the mutual impedance in CST Microwave Studio ^{TM} as we decreased the radius of the receiver coil. Figure 2.11 shows the results of simulating the mutual impedance between coils, when the receiver coil radius is swept from 0.5 cm to 2 cm, the transmitter coil radius was 2 cm, coil to coil separation was 4 cm, and the metamaterial to transmitter separation was 5 mm.

As seen in Figure 2.11, the metamaterial produces a large enhancement in the mutual impedance between the coils even when the receiver coil radius is reduced. This result is expected, since a reduction in the receiver coil radius only reduces the area over which the flux is seen, but the metamaterial flux enhancement is independent of the receiver coil area.

2.5 Results

In order to further optimize our system efficiency, the metamaterial sample position that results in the largest possible mutual impedance needs to be identified. The optimal metamaterial sample position needs to be found experimentally, since: 1) Formulas presented in previous works [11] are not applicable to our system; 2) The extracted material properties that result in the largest efficiency enhancements in our system are different from the perfect lensing properties. The optimal metamaterial position was found through the following procedure: The metamaterial sample was placed in between two 2 cm radius coils; these coils were placed 11 cm apart. Then, the mutual impedance between the coils was measured, when the metamaterial was moved from 3 - 9 cm away from the excitation coil (using the center of the metamaterial as the reference). Figure 2.12 shows the mutual impedance measurements and simulations at 5.574 MHz.

As seen in Figure 2.12, the maximum mutual impedance of the system shows a significant dependence on the metamaterial position. An ideal perfect lensing system would not show any dependence on the position of the material, since a perfect lens metamaterial can be modeled as a reduction on the distance between the coils that is equal to twice the thickness of the metamaterial. In our case though, we are not working at the perfect lensing condition of μ_r' = -1, but at the condition μ_r' = -0.61 where the maximum mutual impedance was observed. It can be seen in Figure 2.12 that the mutual impedance between the coils increases as we move the coil closer to the excitation or receiver coils; therefore we conclude that the optimal placement of the metamaterial is as close to the excitation coil as possible, which due to the limitations of our measurements setup is 5 mm away from the excitation coil. Notice that this position has the benefit of maximizing the working distance of the system as well. The symmetry of the plot shown in Figure 2.12 helps validate the measurement results. The impedance matrix should be symmetric for passive circuits, and as a consequence, the mutual impedance among the coils should be the same regardless of whether we excite the transmitter or receiver coil, or equivalently move the metamaterial sample closer to the transmitter or receiver.

2.5.1 Single Turn System Enhancement

Having shown that our metamaterial sample is capable of increasing the mutual impedance between two coils, and identified the position of maximum mutual impedance, we move on to measure efficiency increases. A 2-coil resonant inductive WPT system was built with the parameters listed in Table 2.2.

As seen in Table 2.2, we decided to add additional lumped elements to the system in order to increase the tunability of its frequency range. Care was taken to make sure that the additional inductors would not influence the mutual coupling of the transmitter and receiver devices and thus affect the results. Table 2.2 also shows that the receiver radius was set to 2 cm. Some applications may require smaller receiver coils, but we chose these radii to decrease sensitivity to errors in coil separation and angular misalignment. As seen in Figure 2.11, our metamaterial sample produces a large enhancement even for smaller coils. Therefore, we expect to see efficiency enhancements similar to the ones presented on this paper even when the received coil is miniaturized.

Figure 2.13 shows the measured and simulated efficiency for the conventional and the metamaterial-assisted systems as a function of transmitter to receiver coil separation. The working frequency was chosen to be the frequency at which the metamaterial caused the largest mutual impedance enhancement, 5.574 MHz. For these measurements, the metamaterial was placed 5 mm away from the excitation coil, which is the minimum separation we could achieve in our measurement setup (mostly due the thickness of the metamaterial and coil holders). Range extension caused by the metamaterial can be found by subtracting the distance at which the metamaterial-assisted system achieves a target efficiency from the distance at which the conventional system achieves the same efficiency. On the other hand, the efficiency enhancement of the system can be found by subtracting the metamaterial-assisted system efficiency from the conventional system efficiency at the same working distance. The working distance for the metamaterial-assisted system can be computed by subtracting 3 cm, the effective metamaterial thickness, from the distance shown in Figure 2.13. Figure 2.3 is included to clarify these definitions.

The simulated results presented in Figure 2.13 were computed using the properties shown in Figure 2.9 and the homogeneous anisotropic model developed in the previous section. The computed results were found using the Equation 2.3 and the mutual

impedance values shown in Figure 2.10.

It can be seen from Figure 2.13 that using the metamaterial resulted in tangible efficiency enhancements. At 1 cm working distance, 1 cm coil to coil separation in air and 4 cm coil to coil separation when using the metamaterial, the system efficiency increased from 20% to 35%, 1.7 times larger than the original. Efficiency enhancement up to 9 times the original system efficiency can be measured at the largest working distances, but at this point the efficiency of the system is very small. Such large efficiency enhancements can be explained by analyzing the WPT efficiency Equation 2.3. It can be seen in this equation that the efficiency of the WPT system has a square dependence on $|Z_{21,eq}|$, which is a linear function of the mutual impedance Z_M. The efficiency of a conventional 2-coil WPT system decays rapidly, since Z_M decays rapidly as working distance is increased. However, in the presence of the metamaterial, the mutual impedance Z_M is greatly enhanced, and therefore, the decay in mutual impedance is not as dramatic as in the conventional WPT system; thus the WPT efficiency decays more slowly when the metamaterial is used.

Simulation and computed results are in good agreement with measurement results as shown in Figure 2.13. The differences can be explained by errors in the computation of the lumped element impedances, errors in the measurements of distances between the devices, and noise.

2.5.2 Multiturn System Enhancement

The system used in the previous subsection helped us analyze all aspects of using metamaterial in wireless power transfer systems in a consistent manner. Nevertheless, that system efficiency is not representative of the efficiency that 2-coil systems are capable of achieving. Because of this, we further analyzed the efficiency enhancements that our design is capable of achieving when paired with higher efficiency multiturn coils. Table 2.3 shows the parameters of this system and Figure 2.14a and 2.14b show the multiturn system measurement setup and results.

As seen in Figure 2.14b, using the metamaterial designed in this paper results in significant enhancements even when the system uses multiturn coils. In particular, it is important to notice that at a working distance 4.5 cm (7.5 cm equivalent coil-coil separation when using the metamaterial), the efficiency is increased to 20% when compared to the

conventional system that has 10% efficiency at the working distance. Furthermore, for an efficiency level above 10%, the coil-coil distance of the system is extended from 4.5 cm to 8.8 cm, an enhancement of 4.3 cm or 95 % of the original range. These measurements stress even further that, despite the low frequency of operation and extremely compact dimensions, the metamaterial sample presented in this paper is capable of realizing tangible efficiency and range enhancements when used in wireless power transfer systems. Finally, Figure 2.14b shows good agreement between simulated and measured results, despite all possible sources of error.

2.6 Conclusions

In this work, we present a metamaterial sample that is compact (6 cm $\times$ 6 cm $\times$ 2 cm), works at low frequencies (5.574 MHz), and produces large WPT efficiency enhancements. An efficiency of 20% in the metamaterial-assisted WPT system, up from 10% in the conventional system, is seen at a distance larger than one diameter of the transmitter coil (4.5 cm). Additionally, it is shown that the same design is capable of extending the coil-coil distance at which 10% or above efficiency is achieved from 4.5 cm to 8.8 cm, a 4.3 cm extension or 95% of the original system range. Larger enhancements are possible through further optimization of the metamaterial and the wireless power transfer system. The ferrite-loaded, solenoid unit cell was the key to attaining these performance metrics. The optimized unit cell achieved a lateral size of $\lambda_0/10{,}766$ and a low resonance frequency (3.35 - 3.50 MHz) when loaded by a 470 μF capacitor. To the best of our knowledge, this unit cell and metamaterial sample are the most compact reported in literature at low-frequency. Yet, this design can be used to provide large WPT efficiency enhancements while maintaining the system working distance. We believe these results indicate a strong future for metamaterials in low-frequency applications, such as biotelemetry systems.

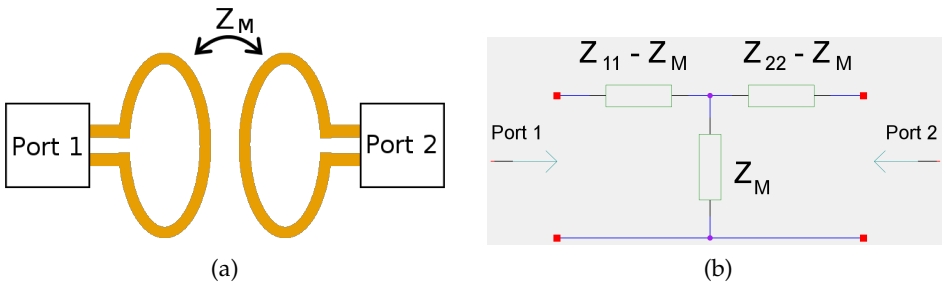

(a) (b)

Figure 2.1: 2-Coil coupling schematic and circuit equivalent. a) Setup diagram, b) 2-port circuit equivalent.

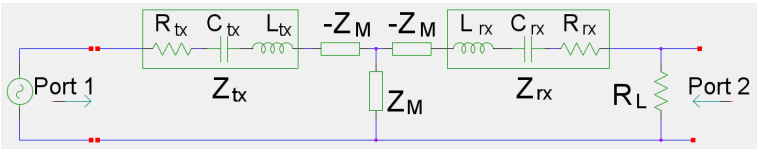

Figure 2.2: 2-coil WPT system circuit diagram.

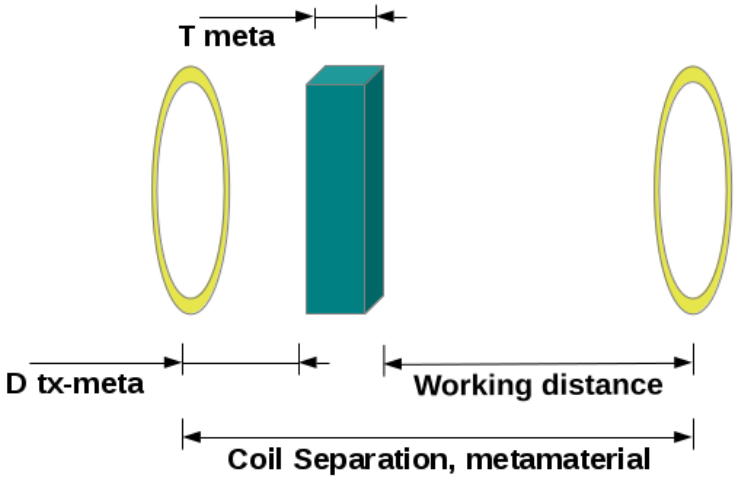

(a)

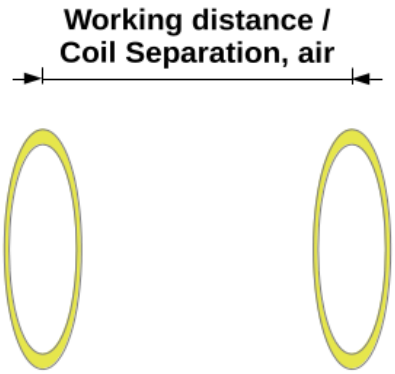

(b)

Figure 2.3: Efficiency measurement setup. a) Efficiency measurement setup using metamaterial design, b) efficiency measurement setup in air.

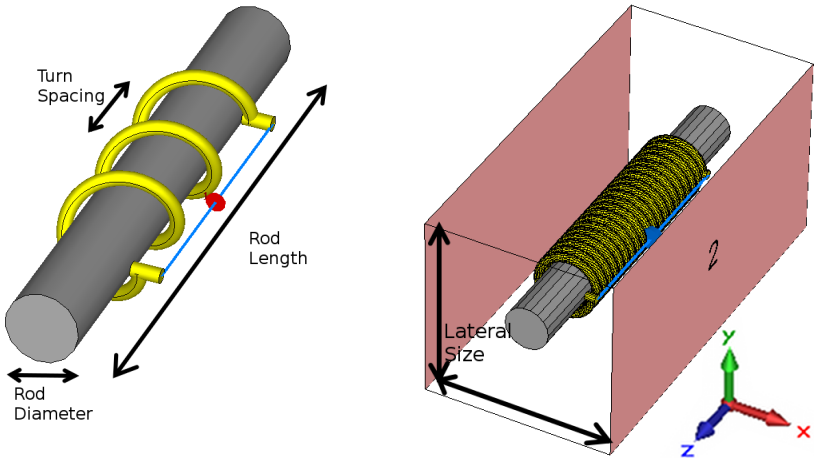

(a) (b)

Figure 2.4: Unit cell diagram and setting for effective property vs. cell spacing study. a) Proposed unit cell, b) setting used for effective property vs. cell spacing study.

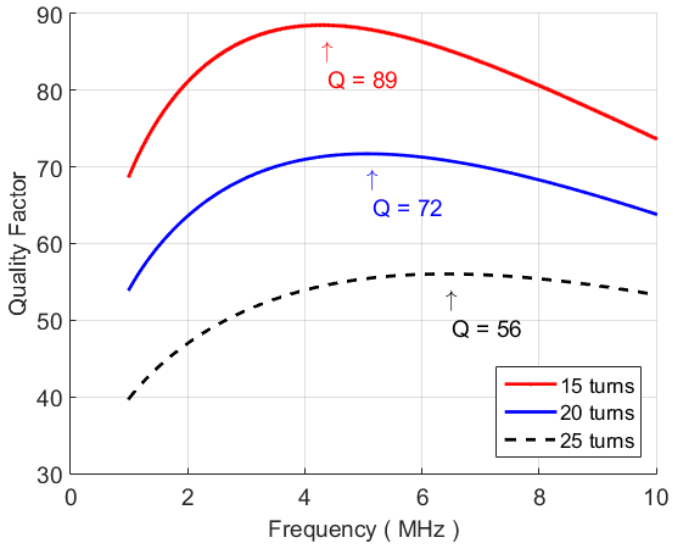

Figure 2.5: Simulated unit cell Q factor vs. number of turns. The simulated ferrite rod had 2 cm in length, 2.5 mm in diameter and a bulk relative permeability of $\mu_r' = 133$.

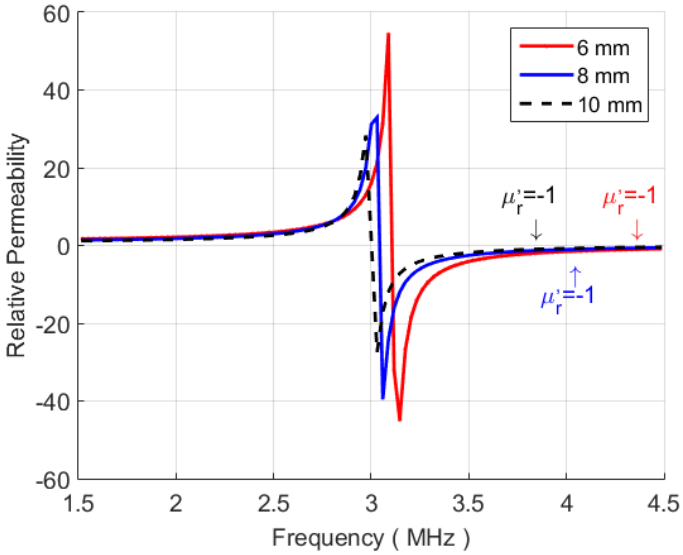

Figure 2.6: Simulated properties of ideal metamaterial vs. unit cell spacing. Unit cell parameters are shown in Table 2.1.

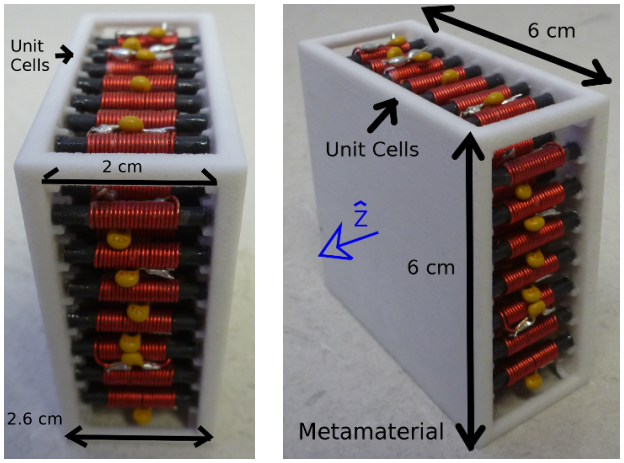

(a) (b)

Figure 2.7: Fabricated metamaterial. a) Side view, b) Perspective view.

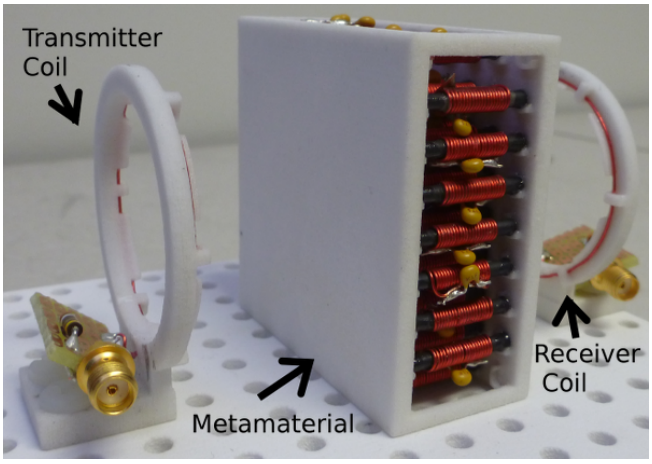

(a)

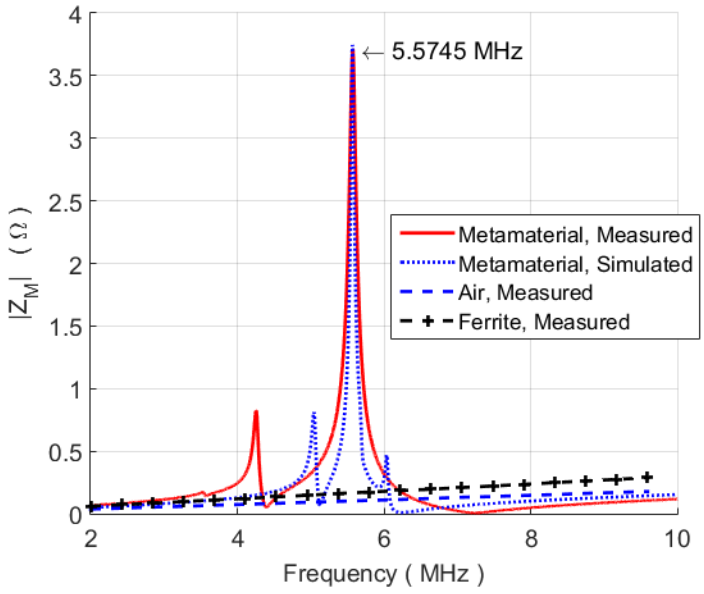

(b)

Figure 2.8: Metamaterial effect on mutual impedance of 2-coil system. a) Mutual impedance measuring setup, b) measured mutual impedance between 2 coils that are 4 cm apart.

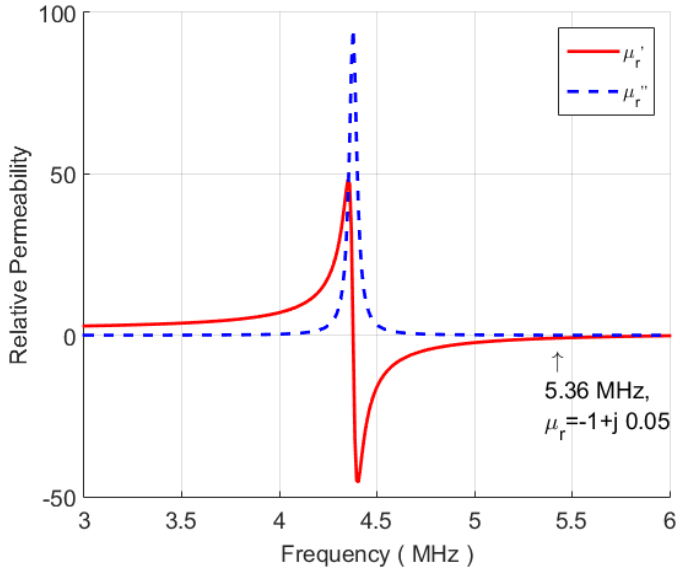

Figure 2.9: Effective material properties of the fabricated metamaterial sample.

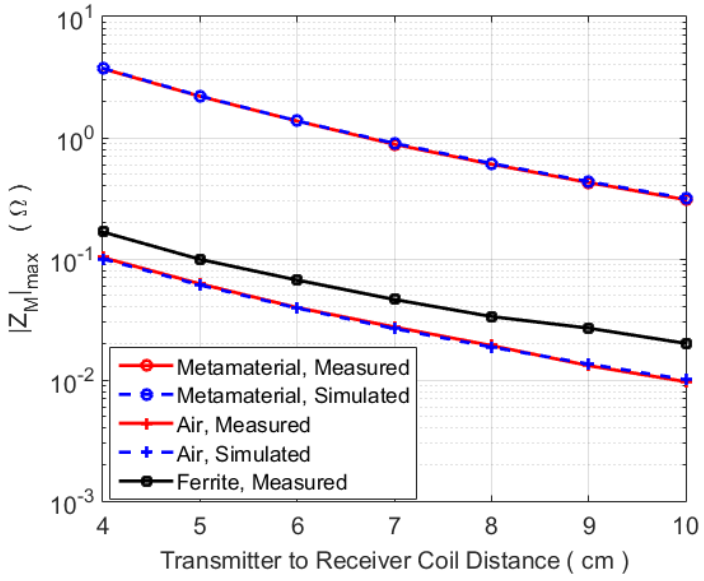

Figure 2.10: Mutual impedance magnitude measurement vs. simulation.

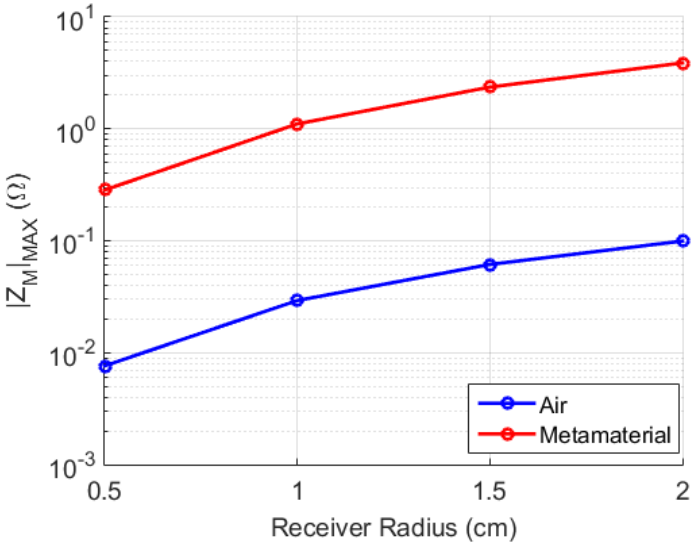

Figure 2.11: Receiver radius effect on mutual impedance enhancement.

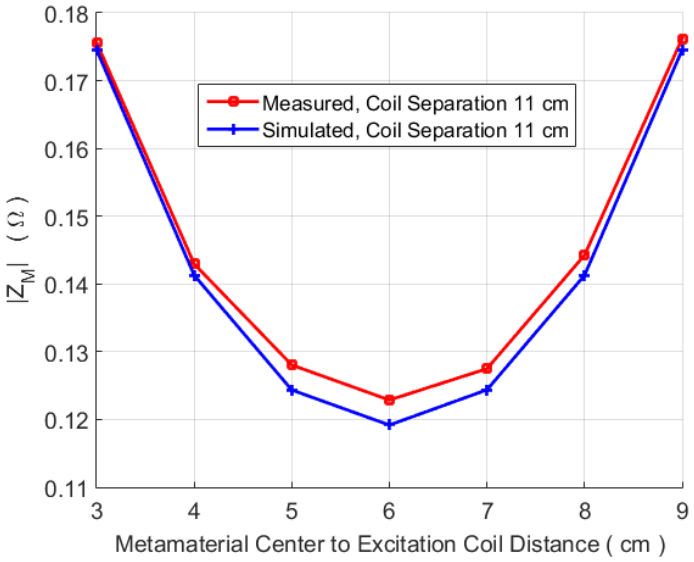

Figure 2.12: Mutual impedance magnitude vs. metamaterial sample position.

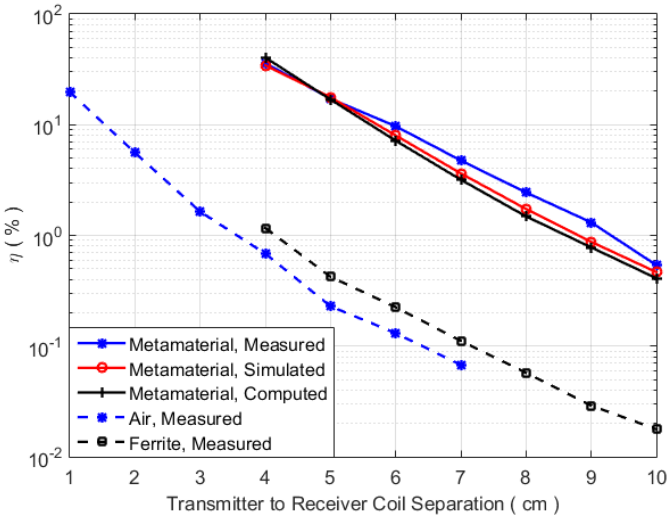

Figure 2.13: WPT efficiency measured as a function of coil to coil separation.

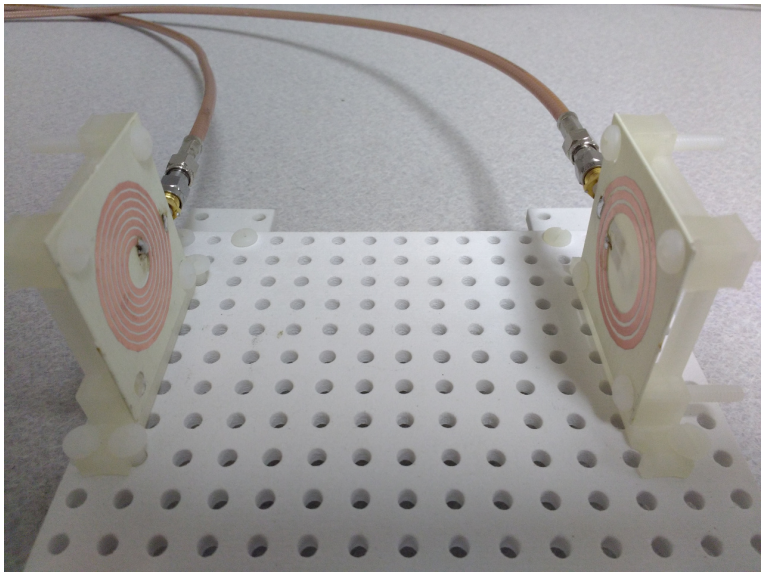

(a)

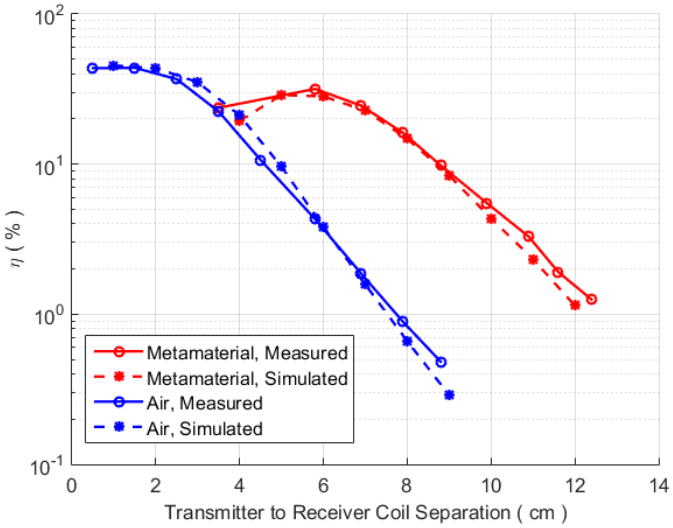

(b)

Figure 2.14: Multiturn system efficiency. a) Measurement setup, b) measured and simulated efficiencies.

Table 2.1: Unit cell parameters.

Parameter	Value
Core material	61 (Fair-Rite, part number: 3061990861)
Core permeability	μ_r' = 133
Core length	2.0 cm
Core diameter	2.5 mm
Solenoid Wire	Copper single strand, 24 AWG
Solenoid Turns	20
Resonating Capacitor	470 μF
Resonance Frequency	3.3 MHz
Q	71

Table 2.2: Single turn WPT system parameters.

Parameter	Transmitter	Receiver
Resonance type	series	parallel
Coil Type	single turn	single turn
Coil Radius	2 cm	2 cm
Coil Wire	24 AWG, copper	24 AWG, copper
Coil Inductance	0.2 μH	0.2 μH
Added Capacitor	300 pF	300 pF
Variable Capacitor	30 -340 pF	30 - 340 pF
Added Inductor	1.9 μH	1.4 μH
Parasitic Resistance	0.8 Ω	0.3 Ω
Load Resistance	N/A	1000 Ω

Table 2.3: Multiturn WPT system parameters.

Parameter	**Transmitter**	**Receiver**
Resonance type	series	parallel
Turns	7	3
Trace Width	1.5 mm	2.0 mm
Outer Diameter	40 mm	40 mm
Inner Diameter	9.7 mm	21 mm
Inductance	1.07 μH	367 nH
Parasitic Resistance	1.18 Ω	0.207 Ω
Load Resistance	N/A	1000 Ω

2.7 References

[1] E. Waffenschmidt and T. Staring, "Limitation of inductive power transfer for consumer applications," in *Power Electronics and Applications, 2009. EPE '09. 13th European Conference on*, Sept 2009, pp. 1–10.

[2] G. Wang, W. Liu, M. Sivaprakasam, and G. Kendir, "Design and analysis of an adaptive transcutaneous power telemetry for biomedical implants," *Circuits and Systems I: Regular Papers, IEEE Transactions on*, vol. 52, no. 10, pp. 2109–2117, Oct 2005.

[3] A. RamRakhyani, S. Mirabbasi, and M. Chiao, "Design and optimization of resonance-based efficient wireless power delivery systems for biomedical implants," *Biomedical Circuits and Systems, IEEE Transactions on*, vol. 5, no. 1, pp. 48–63, Feb 2011.

[4] F. Zhang, X. Liu, S. Hackworth, R. Sclabassi, and M. Sun, "In vitro and in vivo studies on wireless powering of medical sensors and implantable devices," in *Life Science Systems and Applications Workshop, 2009. LiSSA 2009. IEEE/NIH*, April 2009, pp. 84–87.

[5] N. Neihart and R. Harrison, "Micropower circuits for bidirectional wireless telemetry in neural recording applications," *Biomedical Engineering, IEEE Transactions on*, vol. 52, no. 11, pp. 1950–1959, Nov 2005.

[6] J. Park, S. H. Kim, and O. Jeong, "Use case and service framework for wpt (wireless power transfer)," in *Advanced Communication Technology (ICACT), 2014 16th International Conference on*, Feb 2014, pp. 1027–1030.

[7] A. RamRakhyani and G. Lazzi, "On the design of efficient multi-coil telemetry system for biomedical implants," *Biomedical Circuits and Systems, IEEE Transactions on*, vol. 7, no. 1, pp. 11–23, Feb 2013.

[8] A. Kurs, A. Karalis, R. Moffatt, J. D. Joannopoulos, P. Fisher, and M. Soljacic, "Wireless power transfer via strongly coupled magnetic resonances," *Science*, vol. 317, no. 83, 2007.

[9] L. Rindorf, L. Lading, and O. Breinbjerg, "Resonantly coupled antennas for passive sensors," in *Sensors, 2008 IEEE*, Oct 2008, pp. 1611–1614.

[10] B. Wang, K. H. Teo, T. Nishino, W. Yerazunis, J. Barnwell, and J. Zhang, "Experiments on wireless power transfer with metamaterials," *Applied Physics Letters*, vol. 98, no. 25, pp. 254 101–254 101–3, Jun 2011.

[11] Y. Urzhumov and D. R. Smith, "Metamaterial-enhanced coupling between magnetic dipoles for efficient wireless power transfer," *Phys. Rev. B*, vol. 83, p. 205114, May 2011.

[12] Y. Zhao, V. Vutipongsatorn, and E. Leelarasmee, "Improving the efficiency of wireless power transfer systems using metamaterials," in *Electrical Engineering/Electronics, Computer, Telecommunications and Information Technology (ECTI-CON), 2013 10th International Conference on*, May 2013, pp. 1–4.

[13] Y. Zhao and E. Leelarasmee, "Controlling the resonances of indefinite materials for maximizing efficiency in wireless power transfer," in *Electrical Engineering Congress (iEECON), 2014 International*, March 2014, pp. 1–4.

[14] B. Wang, W. Yerazunis, and K. H. Teo, "Wireless power transfer: Metamaterials and array of coupled resonators," *Proceedings of the IEEE*, vol. 101, no. 6, pp. 1359–1368, June 2013.

[15] D. Huang, Y. Urzhumov, D. R. Smith, K. Hoo Teo, and J. Zhang, "Magnetic superlens-enhanced inductive coupling for wireless power transfer," *Journal of Applied Physics*, vol. 111, no. 6, pp. –, 2012.

[16] G. Lipworth, J. Ensworth, K. Seetharam, D. Huang, J. S. Lee, P. Schmalenberg, T. Nomura, M. S. Reynolds, D. R. Smith, and Y. Urzhumov, "Magnetic metamaterial superlens for increased range wireless power transfer," *Scientific Reports*, vol. 4, 2014.

[17] A. L. A. K. Ranaweera, T. P. Duong, and J.-W. Lee, "Experimental investigation of compact metamaterial for high efficiency mid-range wireless power transfer applications," *Journal of Applied Physics*, vol. 116, no. 4, pp. –, 2014.

[18] Y. Fan and L. Li, "Efficient wireless power transfer system by using highly sub-wavelength negative-index metamaterials," in *Wireless Symposium (IWS), 2013 IEEE International*, April 2013, pp. 1–4.

[19] A. Ranaweera, T. P. Duong, B.-S. Lee, and J.-W. Lee, "Experimental investigation of 3d metamaterial for mid-range wireless power transfer," in *Wireless Power Transfer Conference (WPTC), 2014 IEEE*, May 2014, pp. 92–95.

[20] A. Rajagopalan, A. RamRakhyani, D. Schurig, and G. Lazzi, "Improving power transfer efficiency of a short-range telemetry system using compact metamaterials," *Microwave Theory and Techniques, IEEE Transactions on*, vol. 62, no. 4, pp. 947–955, April 2014.

[21] V. G. Veselago, "The electrodynamics of substances with simultaneously negative values of ϵ and μ," *Sov. Phys. Usp*, vol. 10, 1968.

[22] Z. Li, R. Huang, and L. Kong, "Permeability and resonance characteristics of metamaterial constructed by a wire coil wound on a ferrite core," *Journal of Applied Physics*, vol. 106, no. 10, pp. 103 929–103 929–6, Nov 2009.

[23] J. Pendry, "Manipulating the near field with metamaterials," *Opt. Photon. News*, vol. 15, no. 9, pp. 32–37, Sep 2004.

[24] J. Pendry, "Negative refraction makes a perfect lens," *Physical Review Letters*, vol. 85, October 2000.

[25] H. Kim and C. Seo, "Highly efficient wireless power transfer using metamaterial slab with zero refractive property," *Electronics Letters*, vol. 50, no. 16, pp. 1158–1160, July 2014.

[26] S. Lee, S. Kim, and C. Seo, "Design of multiple receiver for wireless power transfer using metamaterial," in *Microwave Conference Proceedings (APMC), 2013 Asia-Pacific*, Nov 2013, pp. 1036–1038.

[27] F. Aznar, J. Bonache, F. Martin, E. Ozbay, K. Alici, F. Bilotti, S. Tricarico, L. Vegni, J. Baena, L. Jelinek, and R. Marques, "Miniaturization and characterization of metamaterial resonant particles," in *38th European Microwave Conference*, Oct 2008, pp. 269–272.

[28] F. Bilotti, A. Toscano, and L. Vegni, "Design of spiral and multiple split-ring resonators for the realization of miniaturized metamaterial samples," *Antennas and Propagation, IEEE Transactions on*, vol. 55, no. 8, pp. 2258–2267, Aug 2007.

[29] K. B. Alici, F. Bilotti, L. Vegni, and E. Ozbay, "Miniaturized negative permeability materials," *Applied Physics Letters*, vol. 91, no. 7, pp. 071 121–071 121–3, Aug 2007.

[30] F. Aznar, J. Garcia-Garcia, M. Gil, J. Bonache, and F. Martin, "Strategies for the miniaturization of metamaterial resonators," *Microwave and Optical Technology Letters*, vol. 50, no. 5, MAR 2008.

[31] W.-C. Chen, C. M. Bingham, K. M. Mak, N. W. Caira, and W. J. Padilla, "Extremely subwavelength planar magnetic metamaterials," *Phys. Rev. B*, vol. 85, p. 201104, May 2012.

[32] M. C. K. Wiltshire, J. Pendry, J. Hajnal, and D. J. Edwards, "Swiss Roll metamaterials - an effective medium with strongly negative permeability," in *Metamaterials for Microwave and (Sub) Millimetre Wave Applications: Photonic Bandgap and Double Negative Designs, Components and Experiments, 2003. IEE Seminar on*, Nov 2003, pp. 13/1–13/10.

[33] E. Gamez, A. Rajagopalan, and G. Lazzi, "Increasing wireless power transfer efficiency on implantable biomedical devices using ferrite based negative permeability metamaterial design," in *2014 USNC-URSI Radio Science Meeting (Joint with AP-S Symposium)*, July 2014, pp. 6–6.

[34] D. R. Smith, D. Schurig, M. Rosenbluth, S. Schultz, S. A. Ramakrishna, and J. B. Pendry, "Limitations on subdiffraction imaging with a negative refractive index slab," *Applied Physics Letters*, vol. 82, no. 10, pp. 1506–1508, 2003.

[35] K. Aydin and E. Ozbay, "Capacitor-loaded split ring resonators as tunable metamaterial components," *Journal of Applied Physics*, vol. 101, no. 2, pp. 024 911–024 911–5, Jan 2007.

[36] D. Ahn, M. Kiani, and M. Ghovanloo, "Enhanced wireless power transmission using strong paramagnetic response," *Magnetics, IEEE Transactions on*, vol. 50, no. 3, pp. 96–103, March 2014.

[37] D. R. Smith, S. Schultz, P. Markoš, and C. M. Soukoulis, "Determination of effective permittivity and permeability of metamaterials from reflection and transmission coefficients," *Phys. Rev. B*, vol. 65, p. 195104, Apr 2002.

CHAPTER 3

ON THE GENERATION OF NONDIFFRACTING BEAMS IN EXTREMELY SUBWAVELENGTH APPLICATIONS

Nondiffracting beams are a class of beams that does not suffer from diffraction. This property is of great interest to a multitude of applications. Most of the work in the literature has focused on applications in the terahertz frequency range. In this chapter, we present a design methodology and implementation that results in low complexity nondiffractive beam launchers in the quasi-static regime, thus allowing a large set of applications to explore and tap the potential of this class of beams.

3.1 Abstract

In this work, extremely subwavelength evanescent Bessel beam launchers are designed, simulated, and experimentally tested to generate nondiffracting beams. The launching apertures consist of several concentric coils strategically positioned to spatially filter the fields of a single actively fed radiating coil. The geometrical properties of each coil element of the aperture were obtained through a procedure based on the Orthogonal Matching Pursuit (OMP) algorithm in order to maximize the quality of the launched beam while minimizing manufacturing complexity. Two apertures with outer diameters of 64 and 48 mm were fabricated and the generated field distributions were measured at the operating frequencies of 13.66 and 13.86 MHz, respectively. Desired and measured field distributions exhibited correlations above 0.9 even as the distance from the aperture was increased, demonstrating the ability of the apertures to approximate the field distribution and harmonic content of a Bessel beam. This work furthers the study and practical implementation of Bessel beams and other types of beams in extremely subwavelength applications such as focusing, wireless power transfer, magnetic stimulation and microwave ablation.

3.2 Introduction

The last couple of decades have seen fast progress in the development of devices that can be characterized as effective mediums, such as metamaterials and metasurfaces. Metamaterials are 3D arrays of regularly spaced subwavelength polarizable particles: the effective properties of metamaterials — permittivity and permeability — arise from the homogenized response of its particles to an applied electromagnetic field. Therefore, control over the metamaterial effective properties can be achieved through careful design of its particles [1]. Metasurfaces, on the other hand, lay out their particles on 2D lattices: this allows for the creation of a sheet with controllable effective impedance [2]. Metamaterials and metasurfaces have been instrumental in the realization of devices that approximate those requiring otherwise unattainable medium properties, such as the perfect lens [3, 4], the invisibility cloak [5], Huygen's surfaces [6], and subwavelength focusing [7] .

In addition to metamaterials and metasurfaces, holographic screens are a third kind of devices that rely on subwavelength elements to control the electromagnetic field. However, unlike metamaterials, holographic screens do not rely on effective medium properties: rather, they exploit the nonhomogeneus response generated by the nonuniform properties and placement of its elements [8]. The objective of holographic screen design is to reproduce a desired electromagnetic field distribution when excited by a driving field. In other words, holographic screens behave like spatial filters that modify the spatial spectrum of a field distribution to generate another. Holographic screens have been used to create apertures that launch beams with exotic properties, such as subwavelength focal spots [9–11], Airy beams [12], Bessel beams [13, 14], etc. Planar construction and direct manipulation of the electromagnetic field are advantages of holographic screens over metamaterial and metasurfaces. In spite of these advantages, holographic screens have not received the same level of attention enjoyed by metamaterials and metasurfaces. This could be due to the difficulty of finding a suitable implementation for these devices. While metamaterials and metasurfaces can be relatively easy to implement when a suitable unit cell is identified and the desired effective properties are known, a procedure that results in low complexity holographic screens for general field distributions, to the best of our knowledge, has not been presented in the literature.

The design, simulation, and experimental validation of holographic screens as spatial

filters for extremely subwavelength applications is explored in this work. A holographic screen consisting of multiple concentric coils is used to filter the field distribution of a radiating coil. The field distribution of the desired aperture will be prescribed to have the functional form of a Gaussian tapered Bessel and a procedure based on the orthogonal matching pursuit (OMP) algorithm is used to obtain a high quality holographic screen with relatively low manufacturing complexity. The system is further simplified to allow for a single driver excitation by exploiting the mutual impedance between the elements. The success of the procedure is then experimentally assessed through measurement of the field correlations at the focal plane and against distance to determine if the generated beam approximates the diffractionless property of the ideal Bessel beam. Section 3.3 presents the methods used in this work. Section 3.4 presents the analysis, design and implementation of the desired holographic screens. Section 3.5 presents the measured results, and Section 3.6 presents the conclusions.

3.3 Methods

The design of holographic screens is generally approached using the following procedure [9,10]: 1) a desired field distribution and a focal plane are chosen; 2) a set of elements is identified; 3) the field distribution of each element is computed and combined in order to reconstruct the desired field distribution; and 4) a suitable implementation is chosen for fabrication. The success of this procedure largely depends on steps 1 and 2. It is evident that not every field distribution can be realized as some may possess nonphysical characteristics. Additionally, even when a field distribution is practically realizable, the quality of the reconstruction largely depends on the physical elements chosen for its implementation. Some choices of elements may result in overly complex holographic screens that are extremely difficult or impossible to implement and fabricate. In the following, procedures for the analysis of general field distributions and for the implementation of high quality and low complexity holographic screens are developed.

3.3.1 Analysis Through Harmonic Decomposition

In order to simplify the analysis of the system, a series of assumptions consistent with the Bessel beam properties will be used. First, the applications considered in this work are

extremely subwavelength; therefore, propagation delays and transmission line effects are negligible and will be ignored. Second, an ideal evanescent Bessel beam is cylindrically symmetric: consequently, the system and its solutions are constrained to show cylindrical symmetry. Third, and in order to simplify resulting expressions, free space will be thought of as a cylindrical waveguide of infinite radius that is aligned with the $\hat{z}$ axis of the system. Fourth, only circular coils will be considered as the possible candidates for the holographic screen construction. The use of a cylindrically symmetric system as well as the desire to work in the extremely subwavelength regime, where the magnetic field is dominant over the electric field for coils, makes this a practical choice. Fifth and final, only planes perpendicular to the $\hat{z}$ axis will be used to prescribe and measure the electromagnetic field. The proposed system is depicted in Figure 3.1.

In a linear time invariant system, any solution to the Maxwell equations can be represented as a superposition of elements extracted from a complete basis that also satisfies Maxwell equations. Using this knowledge and the second and third assumptions above, it follows that any field distribution in the current system can be represented as a superposition of the solutions to the Maxwell equations inside a cylindrical waveguide. These solutions are shown in Table 3.1 for fields propagating along the $\hat{z}$ axis [15].

In Table 3.1, $\beta_z = -j\sqrt{\beta_0 - \beta_\rho}$, with β_0 the wavenumber in free space. It is clear that the value of m in Table 3.1 has to be zero, due to assumptions 1 and 2 (operation in the extremely subwavelength regime and cylindrical symmetry). Additional simplifications are possible if we consider the 4th and 5th assumptions. Because only the field distributions generated by coils are considered, and the measurement plane is constrained to be perpendicular to $\hat{z}$, it is natural to analyze the system through the $\hat{z}$ component of the magnetic field. It is then observed in Table 3.1 that only the transverse electric modes contribute to this field component; therefore, the transverse magnetic components can be safely ignored. These results are then used to write a simplified equation for the distribution of the $\hat{z}$ component of the desired magnetic field at the focal plane H_d in terms of cylindrical harmonics:

$$H_d(z,\rho) = \int_0^\infty \left(-jA_{0n}\frac{\beta_\rho}{\omega\mu\epsilon}C_2 \exp\left(-j\beta_z z\right)\right) J_0\left(\beta_\rho \rho\right) \beta_\rho d\beta_\rho \tag{3.1}$$

Defining the term $\mathcal{H}_d\left(z,\beta_\rho\right) = -jA_{0n}\frac{\beta_\rho}{\omega\mu\epsilon}C_2\exp(-j\beta_z z)$ and substituting it in equation 3.1, results in the following expression:

$$H_d\left(z,\rho\right) = \int_0^\infty \mathcal{H}_d\left(z,\beta_\rho\right) J_0\left(\beta_\rho\rho\right)\beta_\rho d\beta_\rho \tag{3.2}$$

Equation 3.2 is recognized as the inverse Hankel transform of order zero. Therefore, the coefficients $\mathcal{H}_d\left(z,\beta_\rho\right)$ can be found by using the inverse of this function, the Hankel transform of order zero of $H_d(z,\rho)$, also known as the Fourier-Bessel transform [16] :

$$\mathcal{H}_d\left(z,\beta_\rho\right) = \int_0^\infty H_d\left(z,\rho\right) J_0\left(\beta_\rho\rho\right)\rho d\rho \tag{3.3}$$

A great deal of knowledge is gained by decomposing H_d in this manner. This becomes evident by analyzing the effect of changing the focal plane position on the Hankel transform coefficients $\mathcal{H}_d$

$$\begin{aligned}\mathcal{H}_d^{'}\left(z,z',\beta_\rho\right) &= -jA_{0n}\tfrac{\beta_\rho}{\omega\mu\epsilon}C_2\exp(-j\beta_z z')\\ &= \left(-jA_{0n}\tfrac{\beta_\rho}{\omega\mu\epsilon}C_2\exp(-j\beta_z z)\right)\exp\left(-j\beta_z\left(z'-z\right)\right)\\ &= \mathcal{H}_d\left(z,\beta_\rho\right)\exp\left(-j\beta_z\left(z'-z\right)\right)\end{aligned} \tag{3.4}$$

And reconstructing the field distribution at z' by applying the inverse Hankel transform

$$H_d^{'}\left(z,z',\rho\right) = \int_0^\infty \mathcal{H}_d\left(z,\beta_\rho\right)\exp\left(-j\beta_z\left(z'-z\right)\right) J_0\left(\beta_\rho,\rho\right)\beta_\rho d\beta_\rho \tag{3.5}$$

Equation 3.5 is known as the back/forward propagation equation. This equation allows for the computation of the distribution of the $\hat{z}$ component of the magnetic field at any plane and, therefore, explains the properties of the beam generated by the field distribution prescribed at the focal plane. It is easy to validate the nondiffractive property of Bessel beams [17,18] through this equation. The Hankel transform $\mathcal{H}\left(z,\beta_\rho\right)$ of a true Bessel field distribution would have a single nonzero component: propagating this field distribution to any plane z' would result in attenuation of this unique evanescent harmonic and the reconstructed field distribution would remain unchanged. Therefore, a beam with a Bessel field distribution would not suffer diffraction.

Finally, it must be highlighted that the simplifications used herein are applied for convenience. They are not a requirement, and loosening these restrictions and assumptions would result in a more general, but less compact formulation.

3.3.2 Orthogonal Matching Pursuit Implementation

The analysis presented in Section 3.3.1 is useful for understanding the properties of the beam generated by a desired field distribution, but it does not provide guidance in finding a suitable implementation for the required holographic screen. To the best of our knowledge, a procedure to accomplish this task is largely unexplored. In principle, choosing as many elements as possible should always result in a potential implementation. Nonetheless, the quality of the produced field distribution would likely be poor due to the complexity of implementing such a system. Complexity of the system is detrimental as it reduces tolerance to the different sources of error. At low frequencies in particular, complexity could make a system unrealizable, either because it makes the system too large to be of practical use or because it becomes impractical to fabricate and accurately tune each element.

Global optimizers have been used in the past to solve problems where no clear procedure to obtain a viable solution is available [19–21]. Nonetheless, these algorithms are not infallible. Global optimizers tend to fail when the cost function is far from convex [22] — in other words, when the cost function has several local minima. In the problem at hand, holographic screen design, a cost function resembling a convex problem is unlikely to appear. In fact, the shape of the cost function is determined by the properties of the elements used in the optimization, their field distributions and the properties of the desired function. For the general case, the field distribution of the elements in a holographic screen may have a high degree of correlation, implying that several local minima will appear in the cost function. Therefore, finding a suitable solution becomes more complicated as the number of elements required to reconstruct the desired field distribution increases.

An ideal algorithm for holographic screen optimization would yield the minimum complexity solution that best estimates the desired field distribution, even if a large number of elements is required. In other words, an ideal algorithm would yield a compressed representation of the desired field distribution. Many algorithms have been used and

developed for compressed sensing and reconstruction. In this work, we will base our holographic screen design procedure on the orthogonal matching pursuit (OMP) algorithm [23–25]. The algorithm used in this work is described in Figure 3.2.

Figure 3.2 shows the holographic screen optimization algorithm used in this work. The algorithm starts by defining a group of elements E_n for $n = 1, 2, \cdots N$, that are candidates to be included in the holographic screen implementation. Then, the field distribution H_n is computed for each candidate element E_n. Additionally, the desired field H_d is set as the residual error H_e, and an empty solution set is defined $S = \{\varnothing\}$. In the second step, the element E_m whose field distribution H_m better correlates to the residual error H_e is found. Then, the new residual error H_e is computed using $H_m - H_m|S$, the information provided by the new element. H_m is then added to the solution set S, and the procedure is repeated until the maximum number of elements N_{MAX} or the desired error magnitude err_{MAX} have been reached.

Once the optimal set S has been found, the optimal element excitations are obtained by solving the estimation problem [26]$I = R_{ss}^{-1} V_{sd}$, where R_{ss} is the auto-correlation matrix for the field distributions of the elements in S, and V_{sd} is the cross-correlation between the field distributions of the elements in S and the desired field distribution H_d.

3.3.3 Single Port Implementation

Implementing the solution obtained in Section 3.3.2 would require a driver circuit design that is capable of efficiently setting the appropriate excitations for each element of the holographic screen. This is not always convenient, although it could result in a system where the bandwidth is only limited by the self-resonance of its elements, the bandwidth of the driving circuitry, and the frequency range where the quasi-static approximation is valid. A single port implementation similar to the implementations used in previous works is used herein [27–29]. We start by modifying the impedance matrix of the system

$$V = \begin{bmatrix} Z_{11} + Z_{L1} & Z_{12} & \cdots & Z_{1N} \\ Z_{21} & Z_{22} + Z_{L2} & \cdots & Z_{2N} \\ \vdots & \vdots & \ddots & \vdots \\ Z_{N1} & Z_{N2} & \cdots & Z_{NN} + Z_{LN} \end{bmatrix} I \tag{3.6}$$

where V is a $N \times 1$ vector containing the voltage provided to each element, Z_{nm} for $n,\ m = 1,\ 2,\ \cdots,\ N$ are the self and mutual impedances of the elements in the system, Z_{Ln} for $n = 1,\ 2,\ \cdots,\ N$ are the loaded impedances of the tuning circuits, and I is a $N \times 1$ vector containing the current flowing through each element. The vector I is known in this particular case, because it is the solution from the estimation problem in Section 3.3.2, and the elements considered for implementation are coils. A single active element implementation will be considered to further simplify the holographic screen fabrication.

The matrix in Equation 4.1 can be broken down into N independent equations, if it is assumed that losses are negligible and therefore the desired currents can be induced into each coil regardless of the induced voltage. Using this assumption, the value of the loading capacitor C_n for $n = 1,\ 2,\ \cdots,\ N$ can be found as follows:

$$\begin{array}{ll} Z_{Tn} & = \left(V\left(n\right) - \sum_{m=1,m\neq n}^{N} Z\left(n,m\right) I\left(m\right)\right) / I\left(n\right) \\ C_n & = 1/\left(\omega_0 \mathrm{Im}\left(Z\left(n,n\right) - Z_{Tn}\right)\right) \end{array} \tag{3.7}$$

where V in equation 3.7 is an array of zeros except for the element that is actively driven in the single driven port case. The amplitude of the field distribution can be enhanced by increasing the current flowing through the driving coil. This can be accomplished by tuning the driving coil to resonance; the field generated by the holographic screen would be unaffected as it only depends on the ratio between the excitations of each element, not its actual value. The value of the tuning capacitor C_{Tn} can be found as follows:

$$\begin{array}{ll} Z_t & = V\left(n\right) / I\left(n\right) \\ C_e & = 1/\left(\omega_0 \mathrm{Im}\left(Z_t\right)\right) \\ C_{Tn} & = \left(C_e^{-1} + C_n^{-1}\right)^{-1} \end{array} \tag{3.8}$$

where n is the index of driver coil.

3.4 Analysis, Design, and Implementation

The results from Section **??** will be used in the following in order to design and fabricate a holographic screen that launches a diffractionless beam.

3.4.1 Holographic Screen Design

A holographic screen that generates an ideal evanescent Bessel field distribution would result in a diffractionless beam as discussed in Section 3.3.1. Nonetheless, the Bessel function has sidelobes that approach zero asymptotically: therefore, implementing this field distribution would require a holographic screen that is ideally infinitely large. Previous works have dealt with this issue by using a Gaussian taper on top of the Bessel function [13]. The prescribed distribution of the $\hat{z}$ component of the magnetic field is then defined as:

$$H_d\left(z=3,\rho\right)=J_0\left(\beta_d\rho\right)\exp\left(-a^2\rho^2/2\right) \tag{3.9}$$

where $\beta_d = 601.6158$ (rads/m) and $a = 300/5$ (1/m) will be used for convenience. These parameters were chosen to limit the outer diameter of the holographic screen to about 5 cm for the chosen focal plane. The holographic screen will be designed for an operating frequency of 13.56 MHz and its focal plane will be located at $z = 3$ mm. Figure 3.3a shows the cylindrical harmonic composition for the ideal Gaussian tapered Bessel beam and a single turn coil with radius 2.1 mm.

As seen in Figure 3.3a, the Gaussian tapering broadens the cylindrical harmonic composition of the ideal Bessel function. This is to be expected because, for these functions, the Hankel transform of a product is the convolution of the Hankel transform of each term, and the convolution is a spreading function. This spread in the harmonic composition of the Gaussian tapered Bessel beam indicates that this function is no longer truly diffractionless; different harmonics will decay at different rates and the reconstructed field distribution will change from one plane to another. Nonetheless, if the spread in the harmonic composition is sufficiently narrow, the resulting field distribution would approximate a diffractionless beam. This is the case for the parameters chosen in equation 3.9, as seen in Figure 3.3b, where the desired beam has been forward propagated using equation 3.5. The single turn coil field distribution corresponds to a coil with 2.1 mm radius, the coil that best estimates the desired field distribution by itself. Figure 3.3b has been normalized as follows:

$$H_z\left(z=z',\rho\right) = H_z\left(z=z',\rho\right) \,/\, \max\left(H_z\left(z=z',\rho\right)\right) \tag{3.10}$$

This normalization is required to correctly assess the field distribution at different planes, since an evanescent Bessel beam suffers attenuation as predicted by equation 3.5. The beam would suffer phase delay only if it was not evanescent.

A holographic screen capable of generating the Gaussian tapered Bessel beam is now designed. In this specific example, the focal plane is prescribed to be at $z = 3$ mm. The candidate elements for this design will be the concentric filamentary coils with radii in the range of 1.0 to 25.0 mm. Their field distributions are computed analytically using the results from [30]. Figure 3.4 shows the estimation error against the number of elements used in the holographic screen implementation for different optimization strategies.

All strategies use the same range for the filamentary coils, radii 1.0 to 25.0 mm. The range has to be discretized in order to use the OMP method; therefore a step of 0.1 mm was used. In Figure 3.4, the lowest error obtained from 10 runs of the particle swarm with 201 iterations and 10 seeds each was recorded. As seen in Figure 3.4, the particle swarm optimizer (PSO) and the OMP performance is identical for one and two elements. The PSO shows a smaller estimation error until about five elements, when the estimation error becomes almost constant. For a large number of elements, the particle swam estimator is incapable of yielding a solution even though the global minimum has not been reached since the OMP algorithm yields solutions with smaller errors. This happens because the autocorrelation matrix becomes ill-conditioned when the correlation between the field distribution of its elements is large. As the number of desired elements increases the probability of finding at least two strongly correlated elements increases rapidly, which affects the performance of particle swarm. The OMP based algorithm on the other hand does not show the same issue within the range under consideration, indicating that using this algorithm instead of PSO could be beneficial in cases where achieving the desired error requires a large number of elements. The OMP based algorithm has another advantage, in that the elements returned by this algorithm are sorted by their contribution to the desired field estimation. This suggests that a higher tolerance holographic screen could be obtained from this procedure, since errors introduced by the fabrication of the elements with the lowest contributions would not affect the contribution of the higher correlated

elements. PSO does not guarantee such a property. Choosing coils with equally spaced radii is never the optimal strategy according to the results shown in Figure 3.4.

3.4.2 Holographic Screen Fabrication

Figure 3.5 shows the computed distribution of the $\hat{z}$ component of the magnetic field and harmonic content for the holographic screens obtained from the optimization strategies explored in Figure 3.4 for 6 elements.

As seen in Figure 3.5, the OMP and the PSO resulted in similar field distributions and harmonic compositions. The parameters for the holographic screens used to generate this figure are given in Table 3.2.

In Table 3.2 R_n,I_n are the radius of the coil and excitation current required by the nth element of the holographic screen. The parameters presented in Table 3.2 are sufficient to implement the desired holographic screens, assuming that a driver circuit capable of exciting the desired currents was available. Regardless, we will use the results of Section 3.3.3 and an operating frequency of 13.56 MHz in order to minimize the driving circuitry complexity. There are some potential concerns when applying the results of Section 3.3.3 to the single turn implementation of the holographic screens shown in Table 3.2. For example, the parasitic capacitances and inductances are likely to result in significant detuning of the system; some of the elements presented in Table 3.2 are very small. Therefore, the impedance from these elements may be in the same order as the impedance from parasitic elements. Additionally, depending on the implementation frequency, the required tuning capacitors could be very large, further exacerbating the effects of parasitics and potentially disturbing the desired field distribution. In this work, it was decided to use a multiturn implementation for the coils used in the holographic screen in order to reduce the system sensitivity to parasitic elements. The multiturn coil parameters were chosen in such a way that their average diameter matched the diameter of the single turn implementation presented in Table 3.2. The multiturn holographic screen parameters and the required excitations obtained from solving the estimation problem in Section 3.3.2 are shown in Table 3.3. The impedance matrix of the system was extracted by performing 2-port measurements between all the coils in the holographic screen; then, these values were used in the equations presented in Section 3.3.3 to obtain the value of the tuning capacitors.

In Table 3.3, ID is the inner diameter of the spiral, OD the outer diameter, Nt the number of turns, C the loading capacitor value, V the prescribed excitation voltage, and Id the desired current at each element. Comparing Tables 3.2 and 3.3 reveals that the required current in the multiturn holographic screen implementation is roughly 1/Nt smaller than the current required by the single turn implementation, an additional advantage of this implementation choice. The field distributions and harmonic composition of the multiturn holographic screen were virtually identical to those shown in Figure 3.5. Therefore, the performance of this system was not expected to decrease due to the slightly different harmonic content of each coil. The fabricated holographic screen is shown in Figure 3.6. The coils used in this holographic screen were fabricated by hand and multiple capacitors were used to tune each coil to within 1 pF of the required capacitance. AWG 36 insulated copper wire was used for the coil fabrication, and FR4 substrate was used to provide support for the resulting holographic screen.

3.5 Results

The measurement setup and results are presented in this section.

3.5.1 Field Measurements

A motion stage and a magnetic field sensor were designed in order to carry out the measurements presented in this section. A modified 3D printer was used to automate the field measurements as suggested in other works [31]. The 3D printer was chosen due to its quick movements and submillimeter precision. The magnetic field probe was designed based on the mutual impedance definition and Faraday's law of induction [15]:

$$Z_{21} = \frac{V_2}{I_1} = \frac{\mu_0 \frac{d}{dt} \oint \vec{H} \cdot d_n}{I_1}$$

The mutual impedance for two loosely coupled coils depends only on the time derivative of the surface integral of the normal component of the magnetic field over the receiver coil area, H_z in this case. Therefore, for a small sensor coil, sampling the mutual impedance of coils driven by a pure tone at different points in space would be equivalent to sampling the field distribution of H_z with an uncalibrated probe. The probe did not need to be calibrated since the normalization procedure (equation 3.10) made it unnecessary. The

measurement setup is shown in Figure 3.7. A 5 turn, AWG 36, 2.5 mm inner diameter, ferrite loaded solenoid was used to probe the magnetic field in order to enhance measurement sensitivity, as shown in Figure 3.7c.

A slight detuning in the working frequency is expected, due to the effect of the different parasitics presented in the system. The working frequency of the system was found by computing the correlation of the distribution of the $\hat{z}$ component of the magnetic field versus frequency between the measured H_m, and desired H_d field distributions at the focal plane:

$$correlation = < H_d(\rho) \cdot H_m(z_{fp}, \rho) > / \sqrt{|H_d(\rho)|^2 \cdot |H_m(z_{fp}, \rho)|^2} \tag{3.11}$$

where z_{fp} is the value of z that corresponds to the focal plane. The result is shown in Figure 3.8.

As seen in Figure 3.8, the correlation between H_d and H_m is greater than 0.8 in the frequency range of 13.73 to 14.22 MHz. A maximum correlation of 0.93 is achieved at a frequency of 13.86 MHz. This field correlation is only slightly worse than 0.94, which is the simulated correlation for the 6-element holographic screen obtained from the OMP based design procedure. This result demonstrates that the fabricated holographic screen produces the desired field distribution with low estimation error. Next, the diffractionless property of the generated beam is evaluated. Figure 3.9 shows the measured field at 13.86 MHz after normalization with equation 3.10, and its field correlation to the desired field distribution against separation using equation 3.11.

As seen in Figure 3.9, the measured beam closely resembles the desired beam. A sharp focus is observed for the main lobe of the measured beam and the field correlation between the measured and desired fields shows similar dependance to the simulated field correlation. Figure 3.9 only shows results up to z = 12 mm, because after this distance the measurement quality decreases quickly due to noise and the field distribution becomes distorted due to the imperfect filtering of the harmonic content. From z = 3 mm to 12 mm the measured field has decayed to 1/52 of its original value according to measurements. Such a quick decay is expected for the desired field distribution, because its harmonic content has large β_ρ and at the measured frequency, 13.86 MHz, the field distribution suffers

quick attenuation as predicted by equation 3.5. The issue of rapid decay is addressed in the following subsection.

3.5.2 Reduced Decay Design

The field distribution and beam properties for the holographic screen presented in the previous section matched the analytical results with high accuracy. Nonetheless, the quick decay of the desired beam may limit the applications where such a holographic screen could be of practical use. In this section, we overcome this problem by designing a beam that continues to approximate a diffractionless beam but shows a slower decay. Such a beam is realized by using $\beta_\rho = 259.2$ rads/m in equation 3.9. This change causes the harmonic content of the desired field distribution to shift to smaller values of β_ρ, which results in a slower decaying beam as predicted by equation 3.5. An unintended effect of the shift in harmonic content is the increase in the width of the beam, a tradeoff between sharpness of the desired field distribution and field decay is always required. The realized beam and harmonic content are shown in Figure 3.10.

As seen in Figure 3.10, the desired beam continues to show the diffractionless property of the evanescent Bessel beam. This is particularly evident when we compare it to the field distribution of a single turn coil of radius 3.9 mm, which is the coil that better estimates the desired field distribution by itself. Table 3.4 shows the parameters for the multiturn implementation of the required holographic screen. These parameters were obtained through the same procedure as the parameters of the previous holographic screen: 1) Use the OMP algorithm to find the single-turn coils that better estimates the desired field distribution, 2) Replace these coils by multiturn coils with the same average diameter and solve for the required currents, and 3) Measure the fabricated holographic screen impedance matrix and compute the tuning elements for the 1-port implementation.

The fabricated holographic screen is shown in Figure 3.11.

The working frequency is found by taking the field correlation between the measured H_m and desired H_d fields against frequency, Figure 3.12.

As seen in Figure 3.12, the field correlation between H_m and H_d is larger than 0.8 for the frequency band of 13.56 to 17.1 MHz, a bandwidth of 3.64 MHz. The measured field distributions and their field correlation vs. distance are shown in Figure 3.13.

Once again, as seen in Figure 3.13 the simulated and measured results match with a high degree of accuracy. The measured field distribution shows the diffractionless property of the Bessel beam and the range of distances where the field remains diffractionless has been increased from 1.2 cm to above 3.0 cm. Noise and imperfect filtering affect measurements for larger distances.

3.6 Conclusions

Two holographic screens that are extremely subwavelength in size have been designed in this work. The holographic screens were designed to demonstrate the diffractionless property of the Bessel beam while having different beam widths. The screens work at 13.66 and 13.86 MHz, and their outer diameters are 64 and 48 mm, respectively. Both screens were designed using a procedure based on the orthogonal matching pursuit algorithm (OMP), and a single port implementation in order to reduce fabrication complexity. Field correlations above 0.9 were obtained between the desired and the measured field distributions. Additionally, the correlation between the prescribed and measured field distributions was larger than 0.8 for a bandwidth as large as 3.64 MHz for one holographic screen, indicating the possibility of constructing holographic screens that can prescribe the field distribution over a very large bandwidth. Due to their high accuracy, as well as their low fabrication complexity, it is expected that holographic screens based on the results of this paper will be excellent candidates for extremely subwavelength applications that require precise electromagnetic field control. For example, a holographic screen could be used to tailor the spectrum of a transmitter antenna in a wireless power transfer system, with the objective of obtaining a larger power transfer range (slowly decaying beam) or higher tolerance to misalignment (constant magnetic flux over a prescribed surface). In the area of magnetic stimulation, a compact antenna capable of creating a highly penetrating but localized beam could be helpful for selective neurostimulation. Finally, in the area of microwave ablation, holographic screens could aid the selective ablation of the volume under treatment.

3.7 Acknowledgments

The author would like to thank Dr. David Schurig from the University of Utah for the time he invested in discussions related to this project.

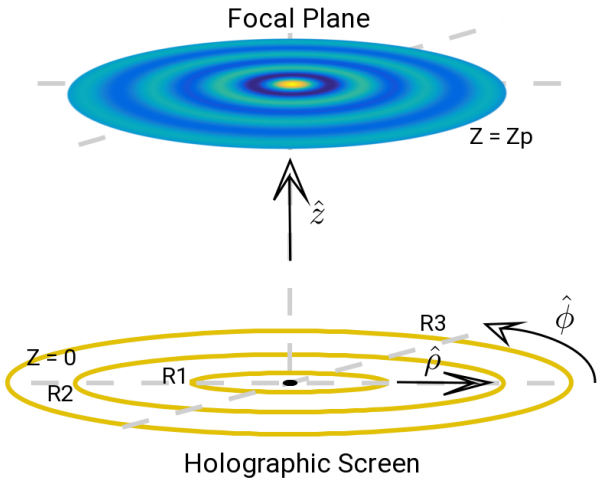

Figure 3.1: Depiction of the proposed system.

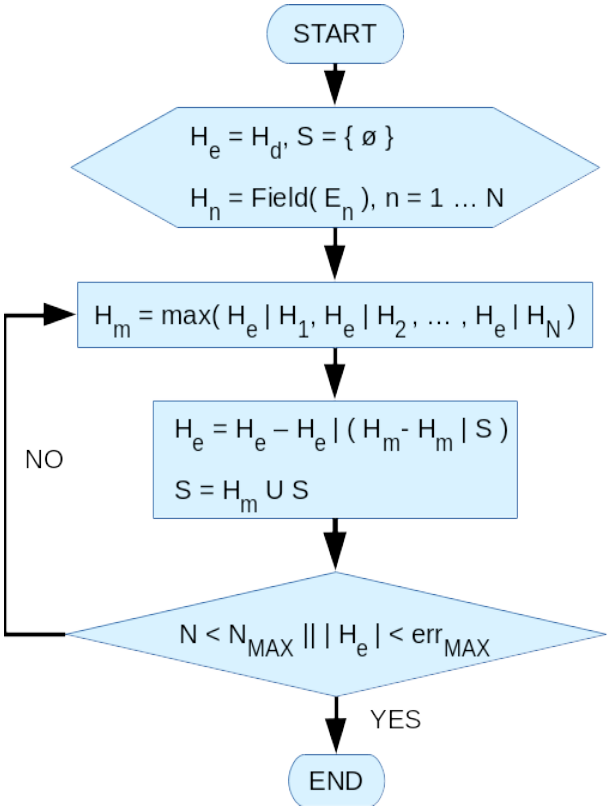

Figure 3.2: Holographic screen optimization procedure.

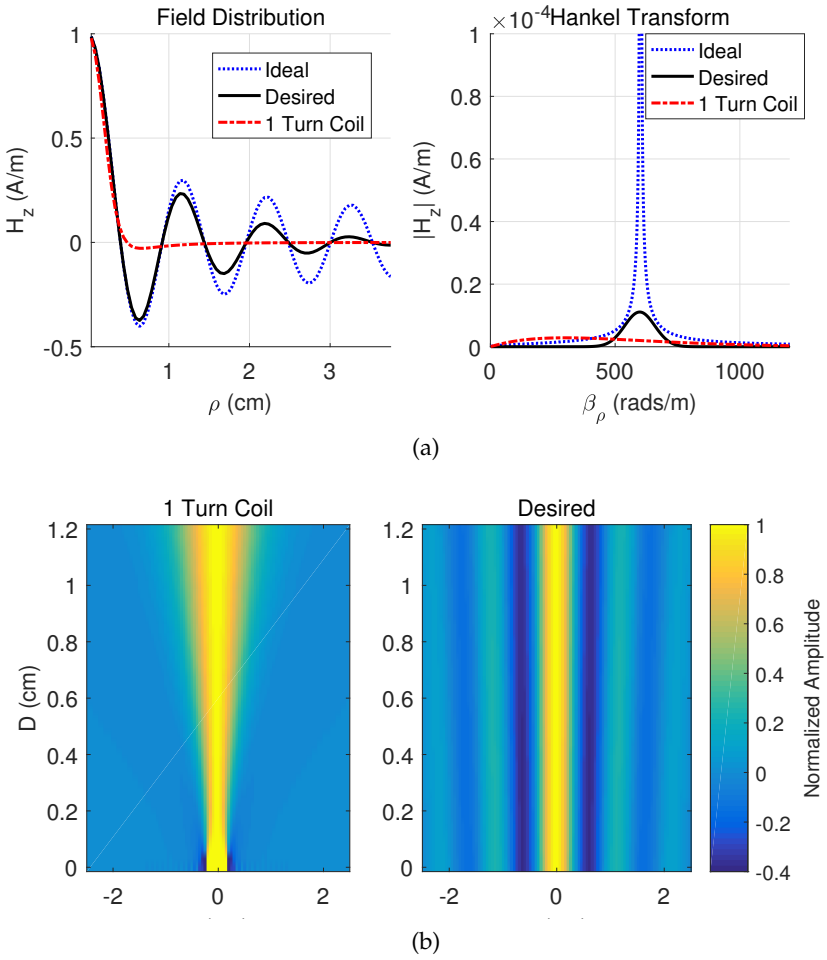

Figure 3.3: Desired Gaussian tapered Bessel distribution of the $\hat{z}$ component of the magnetic field. a) Field distribution and harmonic composition at focal plane, b) cross-section through a plane passing through the diameter of the coil of the normalized forward propagated field.

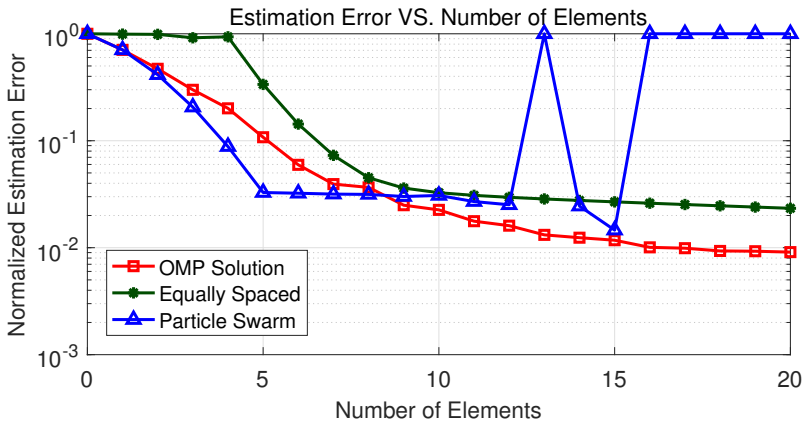

Figure 3.4: Estimation error between desired field distribution and field produced by the holographic screens against number of elements.

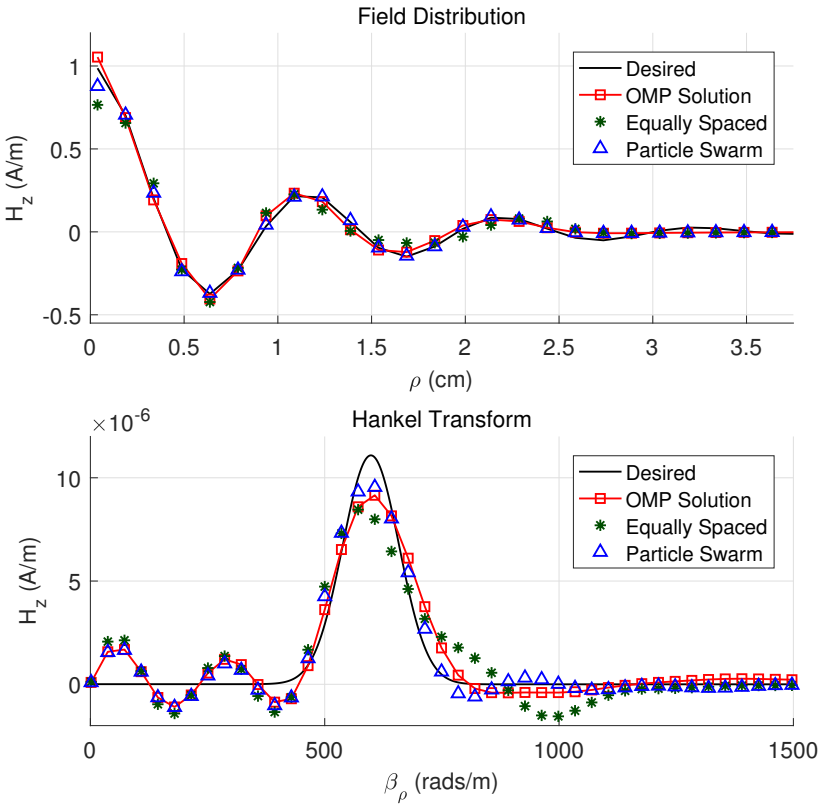

Figure 3.5: Computed distributions and harmonic content for the $\hat{z}$ component of the magnetic field at the focal plane for a 6-element holographic screen.

(a) (b)

Figure 3.6: Fabricated holographic screen. a) Front, b) back

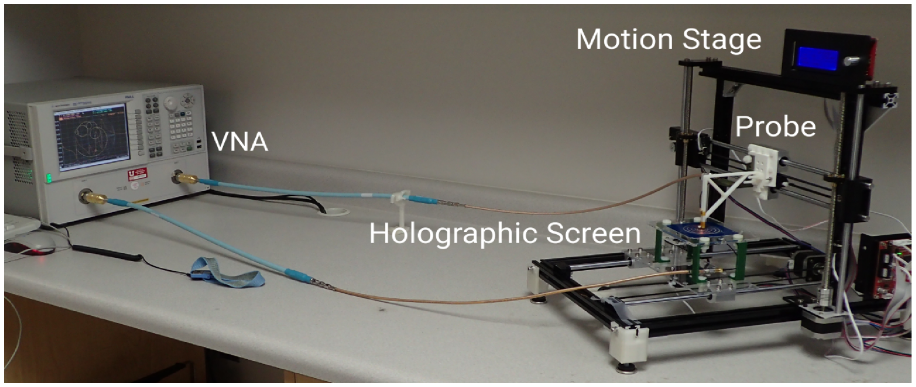

(a)

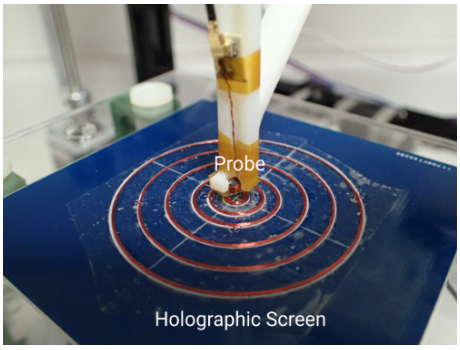

(b)

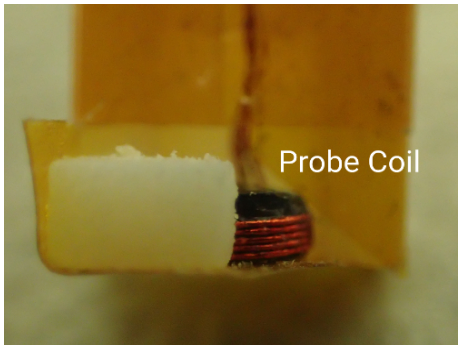

(c)

Figure 3.7: a) Measurement setup, b) measurement probe and holographic screen, c) measurement probe.

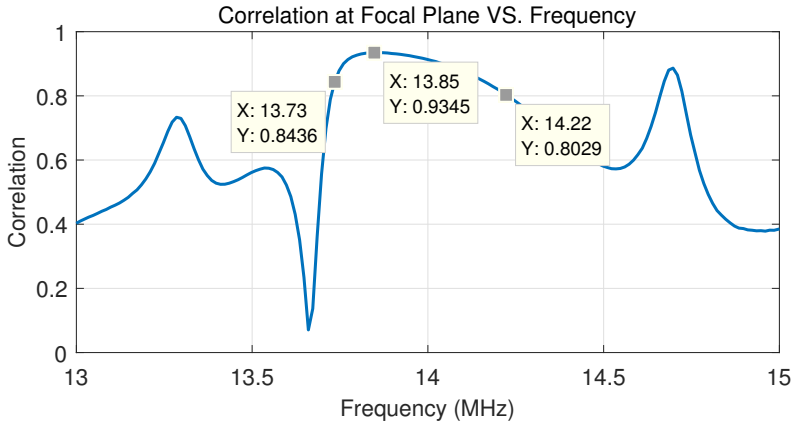

Figure 3.8: Field correlation between measured and desired fields at focal plane versus frequency.

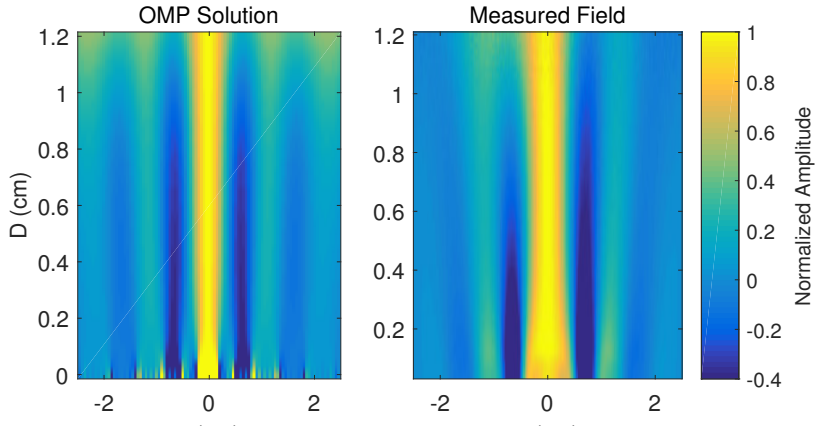

Figure 3.9: $\hat{z}$ component of the measured magnetic fields. a) normalized field, b) field correlation between measured and desired fields against distance from aperture.

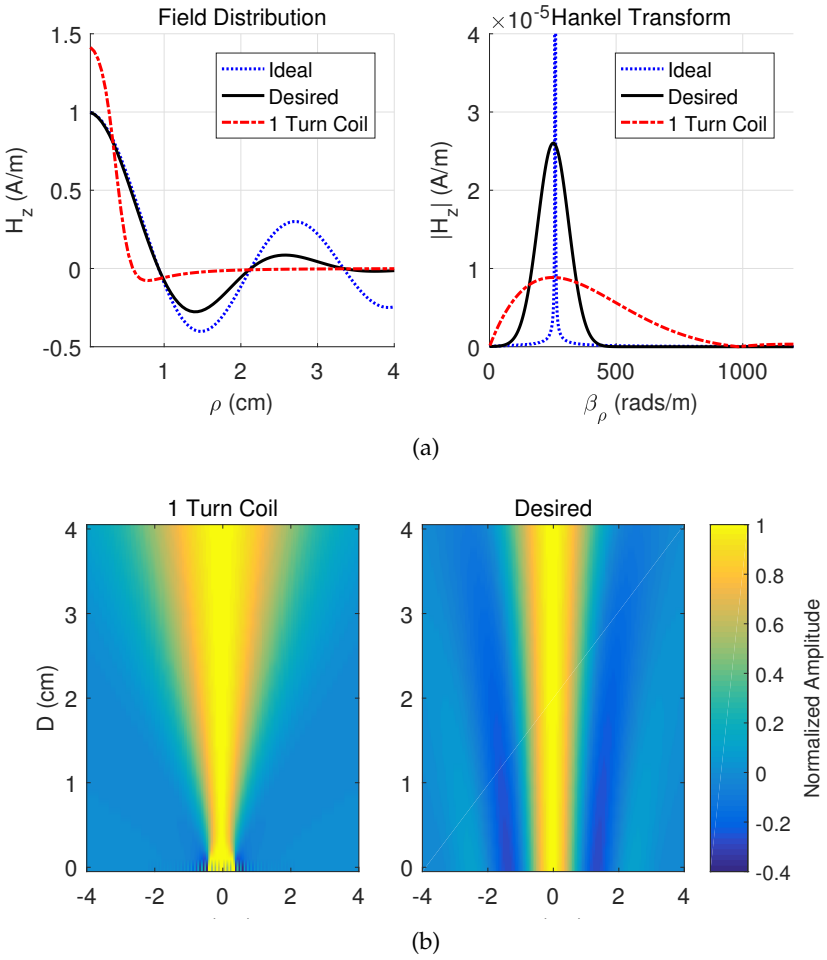

Figure 3.10: Desired Gaussian tapered field distribution of the $\hat{z}$ component of the magnetic field for the reduced decay beam. a) Desired distribution and harmonic content at focal plane, b) normalized forward propagated field.

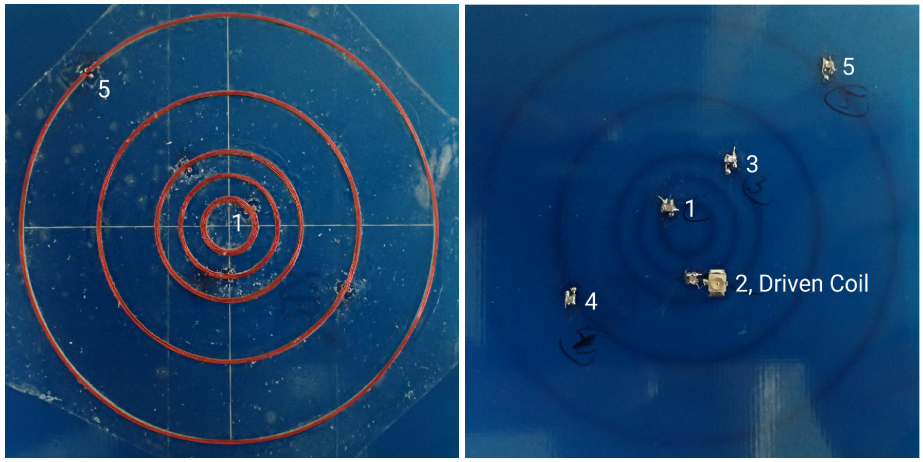

(a) (b)

Figure 3.11: Reduced decay holographic screen. a) Front, b) back

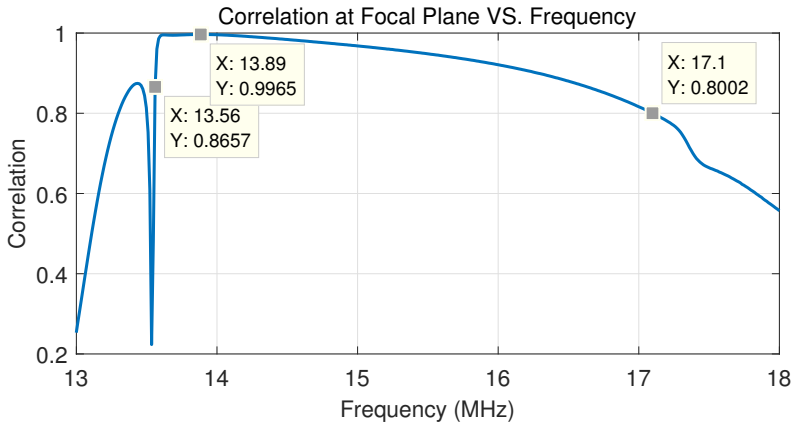

Figure 3.12: Reduced decay holographic screen. Measured to desired field correlation at focal plane versus frequency.

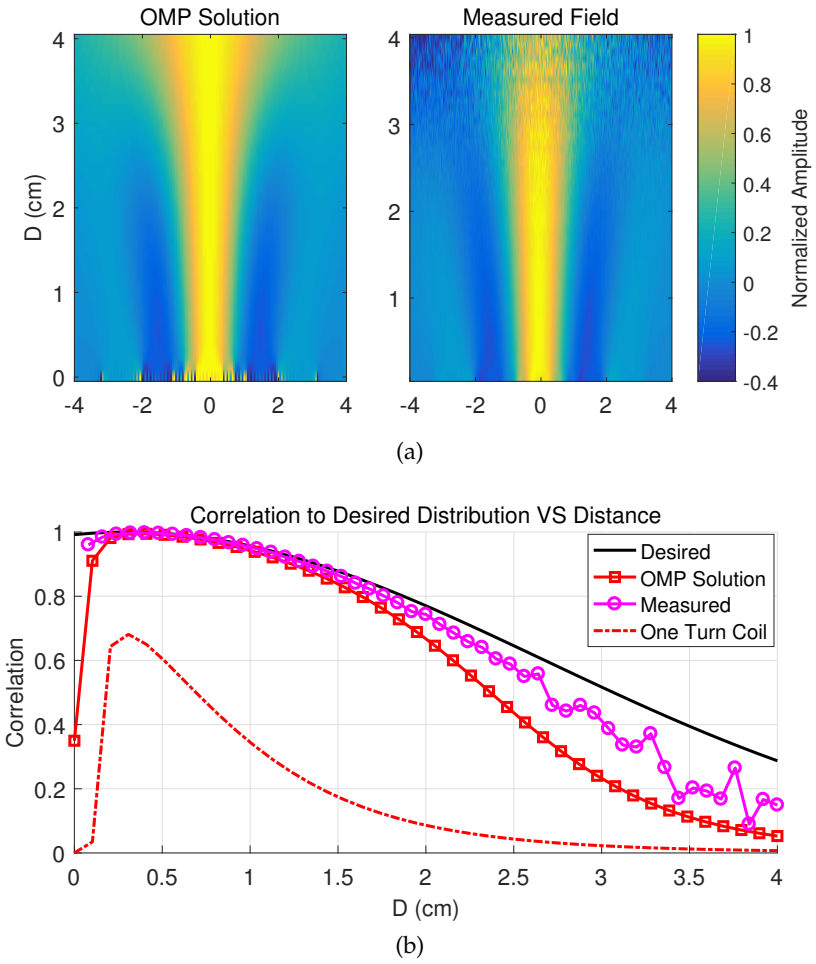

Figure 3.13: Reduced decay holographic screen. a) Measured $\hat{z}$ component of the magnetic field against distance from the holographic screen, b) field correlation between desired and measured field against distance from the holographic screen.

Table 3.2: Parameters for candidate holographic screens

(mm) , (mA)	PSO	OMP	Equally Spaced
R1, I1	3.6, 19.5	2.1, 19.9	4.2, 19.1
R2, I2	8.5, 7.7	5.2, 10.6	8.3, 12.4
R3, I3	9.8, 2.4	8.3, 12.8	12.5, 5.0
R4, I4	14.1, 6.3	13.5, 6.0	16.7, 0.3
R5, I5	19.2, 4.1	18.7, 3.3	20.8, 2.5
R6, I6	23.4, 1.9	23.9, 1.4	25.0, 1.6

Table 3.3: Multiturn holographic screen implementation parameters

	ID (mm)	OD (mm)	AWG	Nt	C (pF)	V (V)	Id (mA)
E1	3.9	4.5	36	4	1,317	1	5.0
E2	10.1	10.7	36	4	480.7	0	2.7
E3	16.3	16.9	36	4	313.2	0	3.2
E4	26.7	27.3	36	4	168.1	0	1.5
E5	37.2	37.6	36	3	207.9	0	1.1
E6	47.6	48.0	36	3	147.2	0	0.5

Table 3.4: Reduced decay multiturn holographic screen implementation parameters

	ID (mm)	OD (mm)	AWG	Nt	C (pF)	V (V)	Id (mA)
E1	7.4	8.2	36	5	252.4	0	1.4
E2	14.5	15.1	36	4	203.1	1	2.3
E3	21.7	22.3	36	4	109.1	0	1.0
E4	39.5	40.1	36	4	93.9	0	1.2
E5	63.0	63.4	36	3	90.0	0	0.4

Table 3.1: Solutions to Maxwell equations inside a cylindrical waveguide.

	TE_{mn}	TM_{mn}
E_ρ^+	$-A_{mn}\frac{m}{\epsilon\rho}J_m\left(\beta_\rho\rho\right)\left[-C_2\sin\left(m\phi\right)+D_2\cos\left(m\phi\right)\right]\exp\left(-j\beta_z z\right)$	$-B_{mn}\frac{\beta_\rho\beta_z}{\omega\mu\epsilon}J'_m\left(\beta_\rho\rho\right)\left[+C_2\cos\left(m\phi\right)+D_2\sin\left(m\phi\right)\right]\exp\left(-j\beta_z z\right)$
E_ϕ^+	$+A_{mn}\frac{\beta\rho}{\epsilon}J'_m\left(\beta_\rho\rho\right)\left[+C_2\cos\left(m\phi\right)+D_2\sin\left(m\phi\right)\right]\exp\left(-j\beta_z z\right)$	$-B_{mn}\frac{m\beta_z}{\omega\mu\epsilon\rho}J_m\left(\beta_\rho\rho\right)\left[-C_2\sin\left(m\phi\right)+D_2\cos\left(m\phi\right)\right]\exp\left(-j\beta_z z\right)$
E_z^+	0	$-jB_{mn}\frac{\beta_\rho^2}{\omega\mu\epsilon}J_m\left(\beta_\rho\rho\right)\left[+C_2\cos\left(m\phi\right)+D_2\sin\left(m\phi\right)\right]\exp\left(-j\beta_z z\right)$
H_ρ^+	$-A_{mn}\frac{\beta_\rho\beta_z}{\omega\mu\epsilon}J'_m\left(\beta_\rho\rho\right)\left[+C_2\cos\left(m\phi\right)+D_2\sin\left(m\phi\right)\right]\exp\left(-j\beta_z z\right)$	$-B_{mn}\frac{m}{\mu\rho}J_m\left(\beta_\rho\rho\right)\left[-C_2\sin\left(m\phi\right)+D_2\cos\left(m\phi\right)\right]\exp\left(-j\beta_z z\right)$
H_ϕ^+	$-A_{mn}\frac{m\beta_z}{\omega\mu\epsilon\rho}J_m\left(\beta_\rho\rho\right)\left[-C_2\sin\left(m\phi\right)+D_2\cos\left(m\phi\right)\right]\exp\left(-j\beta_z z\right)$	$+B_{mn}\frac{\beta\rho}{\mu}J'_m\left(\beta_\rho\rho\right)\left[+C_2\cos\left(m\phi\right)+D_2\sin\left(m\phi\right)\right]\exp\left(-j\beta_z z\right)$
H_z^+	$-jA_{mn}\frac{\beta_\rho^2}{\omega\mu\epsilon}J_m\left(\beta_\rho\rho\right)\left[+C_2\cos\left(m\phi\right)+D_2\sin\left(m\phi\right)\right]\exp\left(-j\beta_z z\right)$	0

3.8 References

[1] D. R. Smith, S. Schultz, P. Markoš, and C. M. Soukoulis, "Determination of effective permittivity and permeability of metamaterials from reflection and transmission coefficients," *Phys. Rev. B*, vol. 65, p. 195104, Apr 2002.

[2] L. Markley and G. V. Eleftheriades, "Meta-screens and near-field antenna-arrays: A new perspective on subwavelength focusing and imaging," *Metamaterials*, vol. 5, no. 2, pp. 97 – 106, 2011, metamaterials Congress - 2010.

[3] J. B. Pendry, "Negative refraction makes a perfect lens," *Phys. Rev. Lett.*, vol. 85, pp. 3966–3969, Oct 2000.

[4] E. S. Gámez Rodríguez, A. K. RamRakhyani, D. Schurig, and G. Lazzi, "Compact low-frequency metamaterial design for wireless power transfer efficiency enhancement," *IEEE Transactions on Microwave Theory and Techniques*, vol. 64, no. 5, pp. 1644–1654, May 2016.

[5] D. Schurig, J. J. Mock, B. J. Justice, S. A. Cummer, J. B. Pendry, A. F. Starr, and D. R. Smith, "Metamaterial electromagnetic cloak at microwave frequencies," *Science*, vol. 314, no. 5801, pp. 977–980, 2006.

[6] C. Pfeiffer and A. Grbic, "Metamaterial Huygens' surfaces: Tailoring wave fronts with reflectionless sheets," *Phys. Rev. Lett.*, vol. 110, p. 197401, May 2013.

[7] D. R. Smith, D. Schurig, M. Rosenbluth, S. Schultz, S. A. Ramakrishna, and J. B. Pendry, "Limitations on subdiffraction imaging with a negative refractive index slab," *Applied Physics Letters*, vol. 82, no. 10, pp. 1506–1508, 2003.

[8] M. F. Imani and A. Grbic, "An analytical investigation of near-field plates," *Metamaterials*, vol. 4, no. 2, pp. 104 – 111, 2010, Metamaterials-2009 Congress in London.

[9] A. Grbic, L. Jiang, and R. Merlin, "Near-field plates: Subdiffraction focusing with patterned surfaces," *Science*, vol. 320, no. 5875, pp. 511–513, 2008.

[10] A. Grbic and R. Merlin, "Near-field focusing plates and their design," *IEEE Transactions on Antennas and Propagation*, vol. 56, no. 10, pp. 3159–3165, Oct 2008.

[11] R. Merlin, "Radiationless electromagnetic interference: Evanescent-field lenses and perfect focusing," *Science*, vol. 317, no. 5840, pp. 927–929, 2007.

[12] M. F. Imani and A. Grbic, "An experimental concentric near-field plate," *IEEE Transactions on Microwave Theory and Techniques*, vol. 58, no. 12, pp. 3982–3988, Dec 2010.

[13] M. F. Imani and A. Grbic, "Generating evanescent bessel beams using near-field plates," *IEEE Transactions on Antennas and Propagation*, vol. 60, no. 7, pp. 3155–3164, July 2012.

[14] M. Ettorre, M. Casaletti, and A. Grbic, "Power link budget for propagating Bessel beams," in *IEEE Antennas and Propagation Society International Symposium (APSURSI)*, July 2013, pp. 960–961.

[15] C. A. Balanis, *Advanced Engineering Electromagnetics*, 2nd ed. John Wiley & Sons, January 2012.

[16] J. W. Goodman, *Introduction to Fourier Optics*. Ben Roberts, 2005.

[17] R. L. Nowack, "A tale of two beams: An elementary overview of gaussian beams and bessel beams," *Studia Geophysica et Geodaetica*, vol. 56, no. 2, pp. 355–372, 2012.

[18] J. Durnin, J. H. Eberly, and J. J. Miceli, "Comparison of bessel and gaussian beams," *Opt. Lett.*, vol. 13, no. 2, pp. 79–80, Feb 1988.

[19] Y. Rahmat-Samii, J. M. Kovitz, and H. Rajagopalan, "Nature-inspired optimization techniques in communication antenna designs," *Proceedings of the IEEE*, vol. 100, no. 7, pp. 2132–2144, July 2012.

[20] R. Poli, J. Kennedy, and T. Blackwell, "Particle swarm optimization," *Swarm Intelligence*, vol. 1, no. 1, pp. 33–57, 2007.

[21] Eberhart and Y. Shi, "Particle swarm optimization: Developments, applications and resources," in *Proceedings of the 2001 Congress on Evolutionary Computation (IEEE Cat. No.01TH8546)*, vol. 1, 2001, pp. 81–86 vol. 1.

[22] M. Clerc and J. Kennedy, "The particle swarm - explosion, stability, and convergence in a multidimensional complex space," *IEEE Transactions on Evolutionary Computation*, vol. 6, no. 1, pp. 58–73, Feb 2002.

[23] Y. C. Pati, R. Rezaiifar, and P. S. Krishnaprasad, "Orthogonal matching pursuit: Recursive function approximation with applications to wavelet decomposition," in *Proceedings of 27th Asilomar Conference on Signals, Systems and Computers*, Nov 1993, pp. 40–44 vol.1.

[24] M. A. Davenport and M. B. Wakin, "Analysis of orthogonal matching pursuit using the restricted isometry property," *IEEE Transactions on Information Theory*, vol. 56, no. 9, pp. 4395–4401, Sept 2010.

[25] T. T. Cai and L. Wang, "Orthogonal matching pursuit for sparse signal recovery with noise," *IEEE Transactions on Information Theory*, vol. 57, no. 7, pp. 4680–4688, July 2011.

[26] S. Haykin and B. Widrow, *Least-Mean-Square Adaptive Filters*. John Wiley & Sons, January 2005.

[27] J. S. Ho, B. Qiu, Y. Tanabe, A. J. Yeh, S. Fan, and A. S. Y. Poon, "Planar immersion lens with metasurfaces," *Phys. Rev. B*, vol. 91, p. 125145, Mar 2015.

[28] M. F. Imani and A. Grbic, "A unidirectional subwavelength focusing near-field plate," *Journal of Applied Physics*, vol. 115, no. 4, p. 044904, 2014.

[29] E. Gámez, D. Schurig, and G. Lazzi, "Using signal estimation for near-field plate optimization," in *IEEE International Symposium on Antennas and Propagation USNC/URSI National Radio Science Meeting*, July 2015, pp. 250–251.

[30] J. M. Griffith and G. W. Pan, "Time harmonic fields produced by circular current loops," *IEEE Transactions on Magnetics*, vol. 47, no. 8, pp. 2029–2033, Aug 2011.

[31] A. Vavoulas, N. Vaiopoulos, E. Hedstrom, C. G. Xanthis, H. G. Sandalidis, and A. H. Aletras, "Using a modified 3d-printer for mapping the magnetic field of {RF} coils designed for fetal and neonatal imaging," *Journal of Magnetic Resonance*, vol. 269, pp. 146 – 151, 2016.

CHAPTER 4

ON THE APPLICATIONS AND INTEGRATION OF SPATIAL FILTERS IN WIRELESS POWER TRANSFER SYSTEMS

Methods for the analysis and design of holographic screens, as well as their optimized implementations, were presented in previous chapters. In this chapter, those results are utilized in order to design a wireless power transfer (WPT) antenna that produces a cylindrically symmetric field distribution. Such an antenna is capable of delivering near constant power to the receiver load at near constant efficiency. This property is of extreme interest in applications where using adaptive compensation systems is not an option, due to cost, complexity, or relatively long adaptation times.

4.1 Abstract

In this work, a wireless power transmitting antenna capable of prescribing a nearly constant magnetic field over a prescribed range is evaluated. Because of this property, this antenna is capable of transmitting nearly constant power at a nearly constant efficiency to the target receiver, regardless of lateral misalignment, even without an adaptive compensation method. The antenna is implemented using a holographic screen which is optimized to reduce losses and to reduce fabrication complexity. Efficiencies in excess of 80% were achieved with nearly constant power delivered to the load, even when the lateral misalignment between the receiver and transmitter coils was as large as 38 mm. A similar coil arrangement from the Wireless Power Consortium Qi standard maintains an 80% efficiency for a lateral misalignment of up to only 19 mm under similar conditions. Nonetheless, power delivery varies drastically for the setup prescribed in the Qi standard. The results shown in this paper can be used in wireless power transfer systems where tolerance to large misalignment is required, but an adaptive compensation method results in an overly complex system, is too costly, or does not adapt quickly enough.

4.2 Introduction

The promise of hassle-free and ubiquitous charging has resulted in wireless power transfer (WPT) systems being integrated in an ever expanding array of systems and devices. Biomedical implants [1–6], wearables systems [7–9], consumer electronics [10–13], and even electric vehicles can now be charged wirelessly [14–18]. In its most common implementation, conventional wireless power transfer systems leverage the inductive coupling between two resonant coils to transmit energy. This method of WPT is commonly preferred to radiative or capacitive WPT schemes, because it does not rely on large electric fields, and consequently reduces power deposition on lossy dielectrics surrounding the transmitter and receiver antennas.

In spite of its advantages, common WPT systems require careful alignment of their coils in order to transfer power efficiently [19]. In general, inductive coupling decreases as the inverse of the distance between the coils cubed, if the coils are kept parallel and concentric. Even larger variations on coupling are seen when angular and lateral misalignment are considered. Matching networks [15], multicoil systems [1, 4], and adaptive compensation systems [5, 6, 19, 20] have been presented as solutions to this problem. Nonetheless, the drastic changes in coupling limit the misalignment tolerance that can be achieved with matching networks and multicoil systems. On the other hand, although compensation systems are theoretically capable of arbitrarily large tolerances, system complexity, cost, and adaptation speed become prohibitively rather quickly.

In this work, we propose the use of holographic screens in order to increase the tolerance to lateral misalignment of WPT antennas. Holographic screens rely on a nonregular array of subwavelength elements to prescribe a desired field distribution at the chosen focal plane [21,22]. A WPT system with large tolerance to lateral misalignment is obtained by prescribing a nearly uniform distribution of the magnetic field at the transmitter coil's focal plane. Simulations validate that this antenna is capable of delivering near constant power to the receiver load with near constant efficiency over the range where the magnetic field is approximately uniform. Discussion on previous works and background material is presented in Section 4.3, the proposed antenna and optimization procedures are presented in Section 4.4, simulation results are presented in Section 4.5, and conclusions are presented in Section 4.6.

4.3 Background

Resonant inductive WPT leverages coupling between two resonant antennas to transmit power. A standard system is shown in Figure 4.1.

In Figure 4.1, an AC power source supplies a voltage V_s to a transmitter antenna, which has inductance L_{TX} and parasitic losses R_{TX}. The system is resonated at the operating frequency ω_0 via a series capacitor C_{TX}. A voltage is induced at the receiver antenna, with inductance L_{RX} and effective parasitic losses are represented by R_{RX}, by virtue of the transmitter and receiver mutual coupling L_M. Usually, a parallel resonant circuit is formed at the receiver by connecting the receiver resonating capacitor C_{RX} and the useful load R_L in parallel to the receiver antenna.

We can write the impedance matrix for the system using the circuit schematic of Figure 4.1.

$$I = \begin{bmatrix} j\omega_0 L_{Tx} + R_{Tx} - j/\left(\omega_0 C_{RX}\right) & j\omega_0 L_M \\ j\omega_0 L_M & j\omega_0 L_{RX} + R_{Rx} + \left(j\omega_0 C_{RX} + 1/R_L\right)^{-1} \end{bmatrix} V \tag{4.1}$$

In Equation 4.1, V is a 2×1 vector containing the transmitter and receiver excitation voltages, I is a 2×1 vector containing the induced currents, and Z is the impedance matrix of the system. The induced current I can be solved for when Z and V are known $I = Z^{-1}V$. From here, the apparent input power P_s, the power deposited in the useful load P_d, and the system efficiency η can be found:

$$P_d = |I\left(2\right)|^2 R_{L\_ser}/2 \tag{4.2}$$

$$P_s = V\left(1\right) I^*\left(1\right)/2 \tag{4.3}$$

$$\eta = |P_d|/|P_s| \tag{4.4}$$

where R_{L_ser} is the equivalent series resistance which can be computed from the following equation:

$$R_{L\_ser} = \mathcal{R}\left((j\omega C_{RX}) \;||\; R_L\right)$$

The optimal parameters for a WPT system are highly application dependent. Nonetheless, the Wireless Power Consortium has released a standard for low power wireless power transfer: the Qi standard [19]. A summary of the main features of the Qi standard is presented in Table 4.1.

The A3 transmitter and the 5W example receiver coils from the Qi standard are chosen in order to set a baseline for the sensitivity of the efficiency and power delivery to lateral misalignment that can be expected from a conventional WPT system. These coils are shown in Figure 4.2a and their parameters are shown in Table 4.2.

Efficiency and power delivered to the load are computed using a transmitter voltage of 5 V and a load resistance of 10 Ω using Equations 4.4 and 4.2. FastHenry, a commercial partial element method, was used to compute self and mutual inductances between the coils for varying lateral misalignment. Delivered power and system efficiency are shown in Figure 4.2b.

As seen in Figure 4.2b, efficiency and power delivery are highly sensitive to lateral misalignment. For a misalignment of just 19 mm along the $\hat{x}$ axis, the efficiency of the system has dropped from 93% to 80%. Within this range, the power delivered to the load has increased from 3.12 W to 19.81 W. More does not always equal better in WPT systems: within this misalignment range, the power delivered to the load has gone from not enough power for the receiver to operate, to an amount of power that will definitely damage and overheat the receiver, if constant voltage is maintained. The problem is only exacerbated if delivered power and efficiency are computed for lateral misalignment along the $\hat{y}$ axis as seen in Figure 4.2b.

In theory, designing an antenna that generates a uniform field magnitude at the desired focal plane would result in a lateral misalignment insensitive WPT antenna. A number of works in literature have presented schemes to create such an antenna [23–28]. Nonetheless, these works fail to consider the need for adjusting the antenna focal plane to the applications requirements. Therefore, the benefits of the antenna design are lost when the focal plane required by the application does not match the proposed antenna fixed focal plane.

4.4 Spatial Filter Design

Holographic screens are nonuniform arrays of subwavelength elements with the capability to control the electromagnetic field at a desired focal plane. Procedures to analyze these systems and find low complexity implementations are outlined in [21] (Chapter 3). The main results from [21] are reproduced here for convenience, but the reader is encouraged to go to [21] for further details.

A number of assumptions are used to develop the equations that follow: 1) the holographic and the prescribed field distributions are assumed to be cylindrically symmetric, 2) the desired field distribution can be decomposed into Bessel harmonics of order zero, 3) propagation effects are negligible because the system operates in the highly subwavelength regime, and 4) the focal plane is always parallel to the desired holographic screen. Using these assumptions, it is found that the desired field distribution H_d of the $\hat{z}$ component of the magnetic field can be decomposed into Bessel zero harmonics through the Hankel transform:

$$\mathcal{H}_d\left(z,\beta_\rho\right) = \int_0^\infty H_d\left(z,\rho\right) J_0\left(\beta_\rho \rho\right) \rho d\rho \tag{4.5}$$

Designing a holographic screen requires the selection of a desired field distribution. In this work, we desire to make a lateral misalignment insensitive WPT system. Examining the definition of mutual impedance provides hints regarding the field distribution that would result in lateral misalignment insensitive WPT:

$$Z_{21} = \frac{V_2}{I_1} = \frac{\mu_0 \frac{d}{dt} \oint \vec{H} \cdot d_n}{I_1} \tag{4.6}$$

where, μ_0 is the permeability of free space, V_2 the voltage excited on the receiver coil due to the transmitter coil current I_1. As seen in equation 4.6, the mutual impedance, and hence the coupling coefficient k, remain constant when the integral of the normal component of the magnetic field across the receiver coil and the transmitter current I_1 are constant. Under these conditions, constant k implies constant efficiency and power delivery. It is then inferred that a WPT antenna capable of producing a cylindrically symmetric step field distribution would result in a misalignment insensitive WPT system. The desired

field distribution for the $\hat{z}$ component of the magnetic field would then be represented by the following function:

$$H_{d-step}(z,\rho) = \begin{cases} 1, & \rho \leq \rho_d \\ 0, & otherwise \end{cases} \tag{4.7}$$

where ρ_d is the radius over which the $\hat{z}$ component of the magnetic field is prescribed to be constant and equal to one.

A cylindrically symmetric step has sharp edges though, and might complicate the creation of a holographic screen that can generate such a field distribution. This happens because sharp edges indicate rich harmonic content, and the desired holographic screen has to provide enough control over the exciting field to reconstruct this content. Because of this, different functions with uniform regions are evaluated in addition to the cylindrically symmetric step. The raised cosine filter is one such function. This function is used in communication systems as a low-pass filter due to its flat pass band gain and fast decaying ripples. This function can be written as:

$$H_{d-rc}(z,\rho) = \begin{cases} 1, & |\rho| \leq \frac{1-\beta}{2T} \\ \frac{1}{2}\left[1+\cos\left(\frac{\pi\rho}{\beta}\left[|\rho| - \frac{1-\beta}{2T}\right]\right)\right], & \frac{1-\beta}{2T} < |\rho| \leq \frac{1+\beta}{2T} \\ 0, & otherwise \end{cases}$$

Another candidate field distribution is obtained by low-pass filtering the cylindrically symmetric step. The Butterworth filter is used to accomplish this task. The desired field distribution is then defined by the following function:

$$H_{d-bw}(z,\rho) = \frac{1}{(1+|\rho|/D_o)^n} * H_{d-step}(z,\rho)$$

where the symbol $*$ represents the convolution operation.

The candidate field distributions and their harmonic content are depicted in Figure 4.3. The parameters used to generate the field distributions shown in this figure are given in Table 4.3.

The value of ρ_d = 47 mm indicates the region where the magnitude of the $\hat{z}$ component of the magnetic field is prescribed to be uniform. This value was chosen because it corresponds to the overall radius of a free positioning system used (A6 transmitter) from the Qi

standard. The focal plane was set at z = 5 mm to match the transmitter-receiver gap used in the reference WPT system presented in Section 4.3.

As seen in Figure 4.3, all of the proposed field distributions have a constant magnitude in the desired range, ρ ¡ 47 mm. Nonetheless, some of them decay faster out of this range, like the cylindrically symmetric step, and others decay more slowly, like the raised cosine filter. Attenuation of the electromagnetic field outside the desired region would be desired, but it is not a requirement to achieve constant power delivery and efficiency. For comparison purposes, Figure 4.3 also shows the field distribution and harmonic content of a single turn coil with 47 mm radius. It can be seen that the field distribution from a 47 mm single turn coil is not a good candidate when the goal is obtaining a field distribution with near constant magnitude over the desired region. Using the field from a single turn coil would result in large variations on the coupling coefficient, and consequently, large variations on power delivery and efficiency.

Now, the goal is choosing the candidate field distribution that results in the simplest implementation. To do this, potential implementations of the candidate field distributions are obtained through the algorithm given in [21] (Chapter 3). This algorithm is shown in Figure 4.4. For convenience, the reader is referred to [21] (Chapter 3) for an explanation of how this algorithm is utilized.

Figure 4.5a shows the field distribution and harmonic content resulting from using the algorithm in Figure 4.4 and 20 elements to estimate the candidate field distributions. As seen in Fig 4.5a, all field distributions closely resemble the desired field distributions. Figure 4.5b shows the field correlation error between the candidate solution and the field distribution generated by its implementation as a function of the number of holographic screen elements. It can be seen in Figure 4.5b that the minimum correlation error between the desired and generated field distributions resulting from the 20-element holographic screen is achieved for the raised cosine field distribution. The raised cosine is then chosen as the field distribution that can be prescribed with the minimum error. The parameters used to construct the holographic screens whose field distributions are shown in Figure 4.5a can be found in Table 4.4.

As seen in Figures 4.5a and 4.5b, the holographic screens with the parameters shown in Table 4.4 produce their prescribed field distributions with very little field correlation error.

Nonetheless, these parameters are not practical for a wireless power transfer system. In particular, it is expected that a holographic screen composed of single turn coils will have a low quality factor. Two operations are then defined to further simplify the candidate holographic screen designs and reduce its losses. These operations are outlined in Figure 4.6a.

Operation 1, Figure 4.6a, consists of replacing every single turn coil in the candidate holographic screen by spirals. In general, this operation has the effect of reducing the required excitation current by the inverse of the turns of the spiral, and increases the quality factor of each element as well. In operation 2, spirals with equal driving current are merged together to facilitate the holographic screen implementation. These operations are likely to increase the holographic screen quality factor and to further reduce fabrication complexity. Nonetheless, these operation use current paths that are not part of the original solution. Therefore, harmonic distortion may be increased significantly if they are not applied wisely.

The candidate holographic screen that generates a raised cosine field distribution, Table 4.4, is then refined by throwing away the coils that result in minimal impact on the uniformity of the field over the prescribed area. Then, the operations shown in Figure 4.6a are applied to the refined holographic screen. The refined holographic screen and its final implementation parameters can be found in Table 4.5. The resulting screens are depicted in Figure 4.6b. In Table 4.5, ID is the inner diameter of the corresponding spiral, OD is its outer diameter, Nt is the number of turns, L the spiral inductance, Q the spiral unloaded quality factor, and the final column shows the driving current required to produce the desired field distribution. Resulting field distributions are shown in Figure 4.6.

As seen in Figure 4.6, the refined and final solution produce an approximate uniform field distribution of the $\hat{z}$ component of the magnetic field. The resulting field distributions are not suppressed beyond the desired uniform space $\rho_d = 47$ mm though. This is a result of throwing away coils with radii > 105.2 mm from the final solution. This decision was made in order to reduce the size of the final holographic screen.

Finally, before the holographic screen design is complete, a way of driving the final design must be devised. For this, the results from [21] (Chapter 3) will be invoked once again. A procedure to drive a holographic screen through a single port is presented in

that work. The reader is encouraged to read those results. The required elements and excitations are shown in Table 4.6. In Table 4.6, C_L is the loading capacitance for the corresponding spiral, and V is the required driving voltage. The operating frequency was chosen to be 140 KHz.

4.5 Results

A low-loss holographic screen capable of producing an approximately constant field distribution for the $\hat{z}$ component of the magnetic field at its focal plane was designed in Section 4.4. The resulting holographic screen relies on tuning capacitors to drive the desired currents as seen in Table 4.5. Because of this, it is reasonable to assume that the frequency range over which the desired field distribution is obtained could be small. This could be an issue because the proposed transmitter antenna is required to be compatible with other antennas from the Qi standard, and under some scenarios, these antennas may work at different frequencies. Figure 4.7 shows the field correlation against frequency between the desired field distribution and the field distribution generated by the proposed holographic screen. It is remarkable that the proposed holographic screen design shows almost no dependence on the operating frequency, for the frequency range used in the Wireless Power Consortium Qi standard, Table 4.1. Such a large bandwidth is attributed to the large difference in the currents required in the spirals used in the final holographic screen implementation, Table 4.5. A large detuning capacitor is required to set the current required in Spiral 1, because the current is small (1 mA), and the spiral has a large quality factor. Because of this, Spiral 1 and Spiral 2 have drastically different self-resonant frequencies. As a consequence, the resonance of Spiral 1 is either above or below the prescribed frequency range.

Finally, delivered power and WPT efficiency are computed for the case where the proposed holographic screen is used in conjunction with the Qi standard 5W receiver coil example. These results are shown in Figure 4.8. As expected, the almost uniform field distribution of the $\hat{z}$ component of the magnetic field results in almost constant delivered power to the receiver load R_L, together with almost constant efficiency. Comparing 4.2b and 4.8 reveals that the lateral misalignment region over which power efficiency is above 80% has increased from 19.74 mm for the Qi standard system to 39.48 mm for the pro-

posed holographic screen system, this region has almost doubled thanks to the proposed system. Power delivery and efficiency remain remarkably constant for the holographic screen system in the region $\rho < 31.96$ mm. No such region can be identified for reference system. Maximum efficiency has been reduced slightly, though, from 93.5% in the standard system, to 86% in the proposed system. It is believed that such a decrease would be more than compensated by the reduction in losses in parts of the system that could be simplified thanks to the proposed design: power amplifiers, matching networks, control logic latency, etc.

4.6 Conclusions

In this work, a holographic screen capable of prescribing a uniform distribution of the $\hat{z}$ component of the magnetic field over a prescribed area is presented. The design was carefully optimized through a modified OMP algorithm to reduce its complexity while maintaining high correlation to the desired field distribution. Then, further refining was applied to reduce implementation complexity even further, and to increase the quality factor of the resulting WPT transmitting antenna. Simulations demonstrate that the resulting WPT antenna delivers almost constant power at almost constant efficiency to the desired receiver load, within the range where the magnitude of the $\hat{z}$ component of the magnetic field is almost constant. Efficiencies in excess of 80% were obtained for large lateral misalignment ranges, up to 39.48 mm. This value is greatly superior to the efficiencies obtained under the same lateral misalignment from a reference WPT system that was extracted from the Wireless Power Consortium Qi standard. The reference antenna has no discernible lateral misalignment region over which power deliver and efficiency are constant. These results are of great interest to systems where, because of complexity, cost, or latency, adaptive compensation schemes cannot be utilized. Dynamic WPT for Electric vehicles and low latency free positioning systems are some examples of such systems.

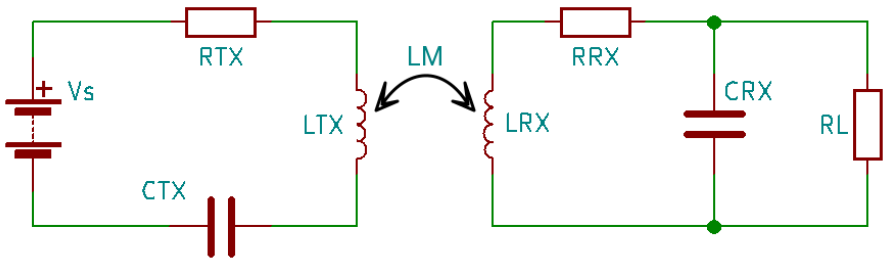

Figure 4.1: Standard wireless power transfer system.

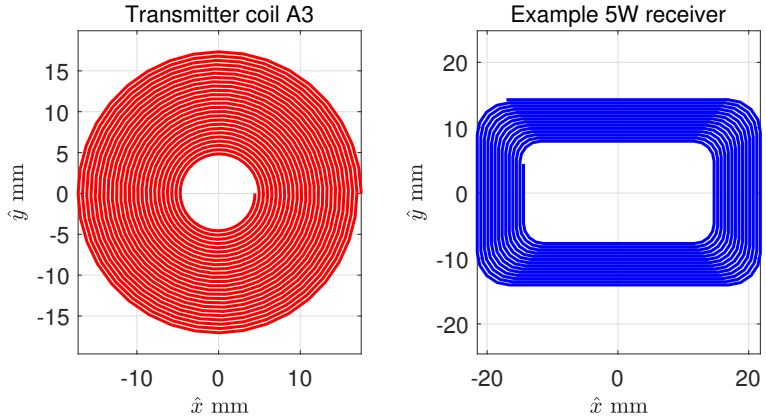

(a) Reference coils from the Wireless Power Consortium Qi standard. A3 transmitter and example 5W receiver coil.

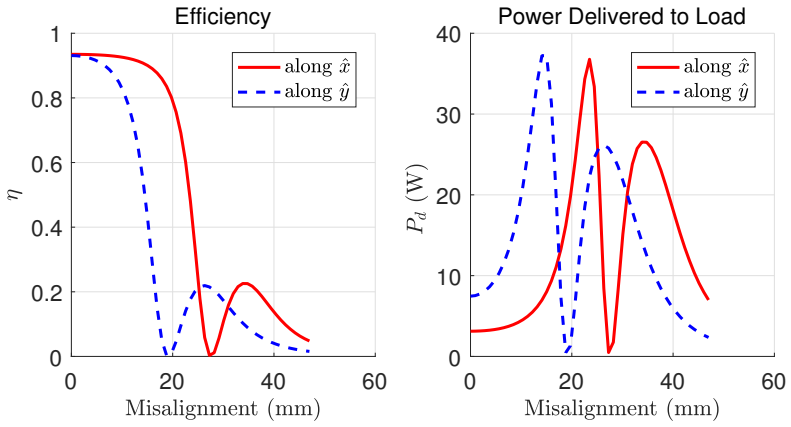

(b) Power delivery and efficiency as a function of misalignment.

Figure 4.2: Wireless Power Consortium Qi standard coils geometry and performance.

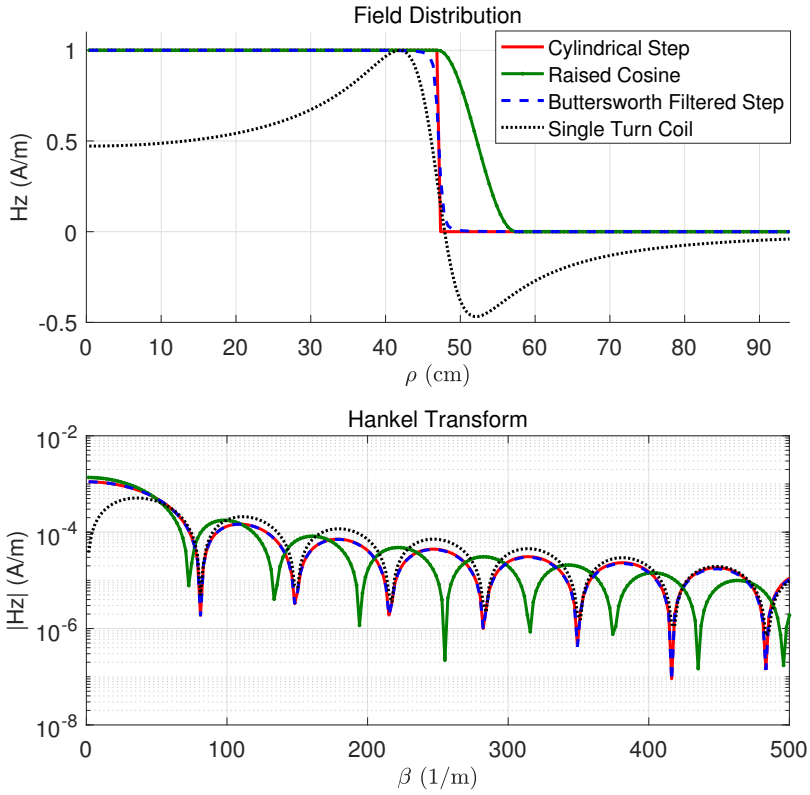

Figure 4.3: Candidate field distributions and their harmonic spectrum.

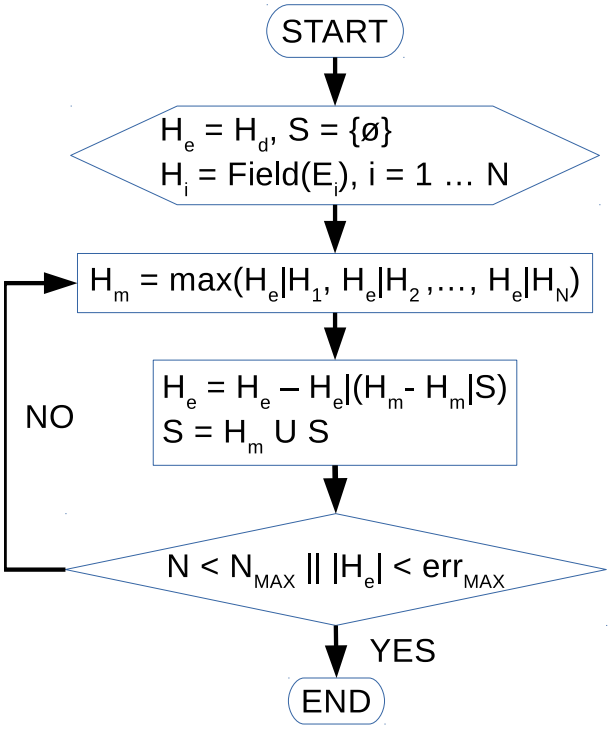

Figure 4.4: Holographic screen optimization flowchart.

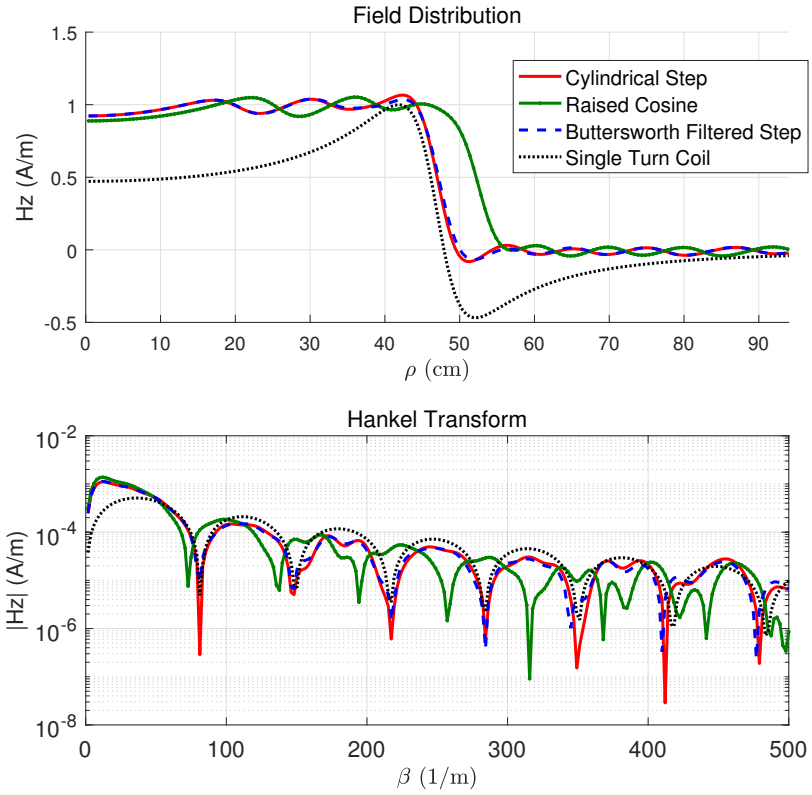

(a) Field distributions and spectrum of potential holographic screen implementations consisting of 20 elements each.

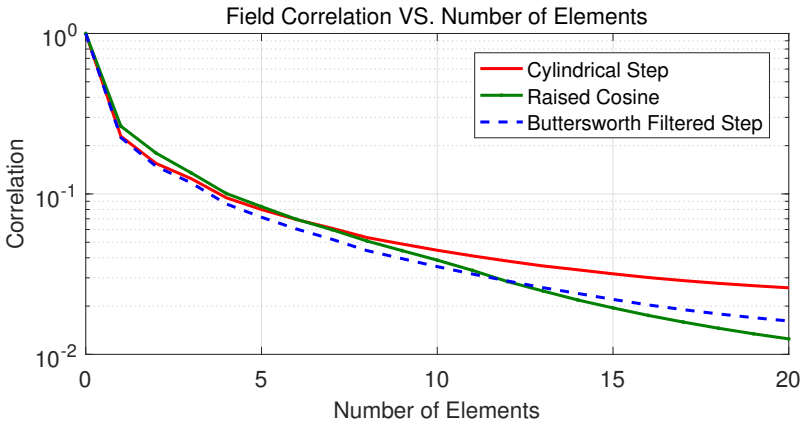

(b) Correlation error against the number of elements used in the holographic screen implementation.

Figure 4.5: Field distribution and correlation error for potential implementations of the desired holographic screen.

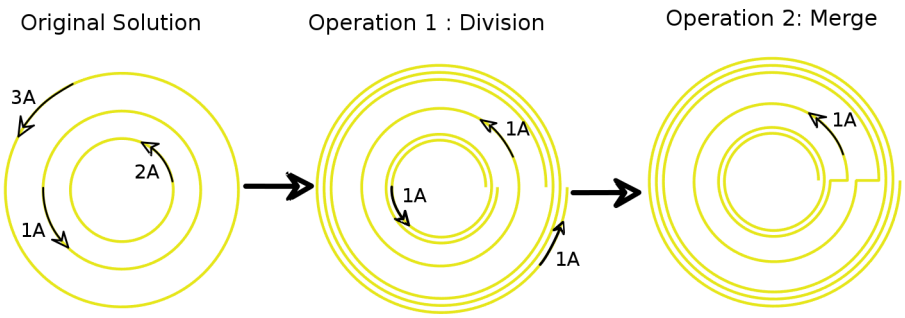

(a) Holographic screens operations. Division consists on replacing single turns for multiturn spirals in order to reduce the driving current. Merging consists in joining coils with the same or similar currents in order to reduce the number of elements that have to be driven and increase the total quality factor.

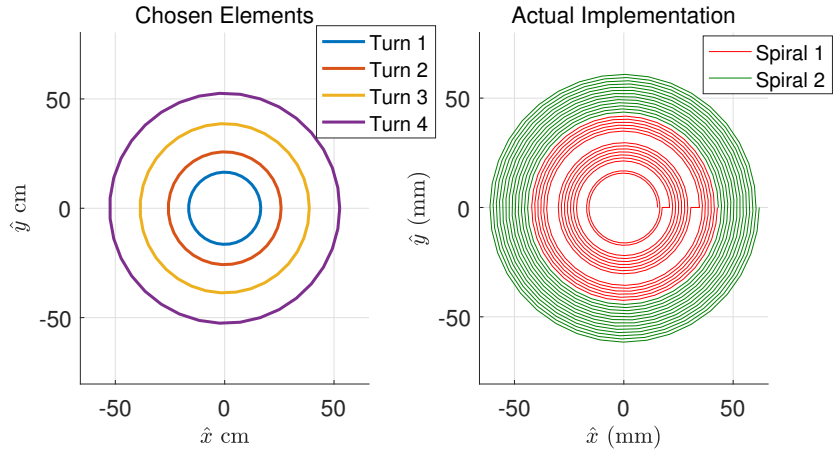

(b) Single turn implementation and multispiral implementation of the desired holographic screen.

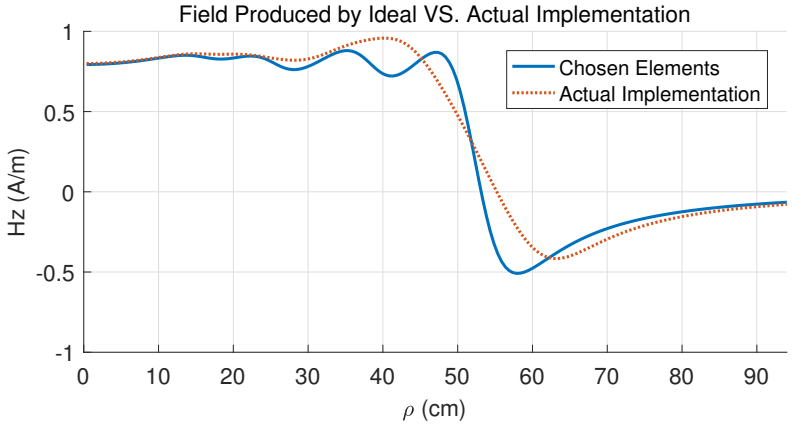

(c) Single turn implementation holographic screen field distribution against multispiral holographic screen field distribution.

Figure 4.6: Chosen solution against actual implementation.

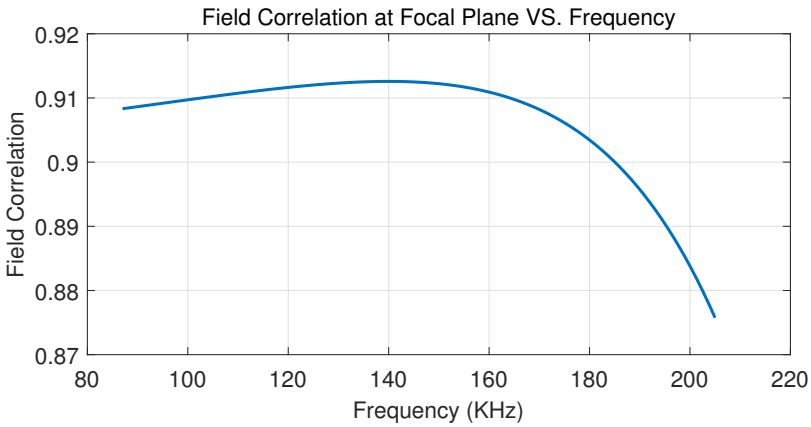

Figure 4.7: Field distribution correlation at focal plane against frequency.

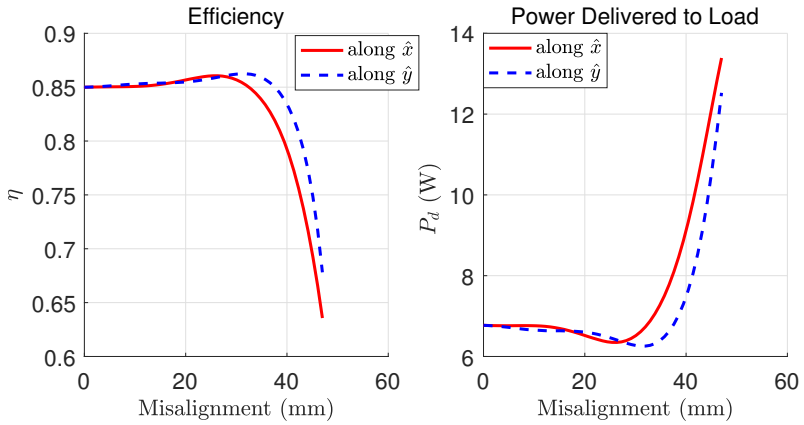

Figure 4.8: Efficiency and power delivery for optimized WPT antenna.

Table 4.1: Summary of features outlined in the Wireless Power Consortium Qi standard.

Operating Frequency	87 KHz - 205 KHz
Baseline Power Transfer	$\leq$5 W
Input Voltage Range	0 V - 12 V
System Efficiency	$\geq$50 % for 10 Ω load
Localization	Guided or free positioning

Table 4.2: Wireless Power Consortium Qi Standard coil parameters.

Parameter	Value
Outer Diameter	33 $\pm$1 mm
Inner Diameter	10$\pm$0.2 mm
Number of Turns	25
Layers	1
Wire	66/40 Litz wire
Inductance	12.4 μH (computed)
Quality Factor	134.3 (computed)
Coil to Surface Distance	2.5 mm

(a) A3 transmitter coil.

Parameter	Value
Outer Length	44.25 $\pm$0.25 mm
Inner Length	28.75$\pm$0.25 mm
Outer Width	30.25 $\pm$0.25 mm
Inner Width	14.75$\pm$0.25 mm
Number of Turns	14
Layers	1
Wire	27/40 Litz wire
Inductance	9.14 μH (computed)
Quality Factor	44.01 (computed)
Coil to Surface Distance	2.5 mm

(b) Example 5W receiver coil.

Table 4.3: Candidate field distributions parameters.

Cylindrical Step		Raised Cosine		Butterworth Filter	
ρ_d	47 mm	β	0.1	D_0	0.5 mm
		T	$\frac{1-\beta}{2\rho_d}$	n	3

Table 4.4: Holographic screen parameters used to generate Figure 4.5a

Cylindrical Step		Raised Cosine		Butterworth Filtered Step	
radius (mm)	current (mA)	radius (mm)	current (mA)	radius (mm)	current (mA)
47.3	+ 43.8	52.6	+ 32.6	47.3	+ 38.2
67.3	+ 5.60	72.0	+ 6.7	67.2	+ 5.9
32.6	+ 7.70	38.7	+ 9.5	32.7	+ 7.4
89.5	+ 3.70	94.5	+ 4.2	89.4	+ 3.7
114.3	+ 2.30	119.6	+ 2.7	114.2	+ 2.3
58.3	+ 8.50	62.4	+ 9.4	58.2	+ 7.6
141.4	+ 1.60	146.9	+ 1.9	141.3	+ 1.6
77.5	+ 4.80	82.4	+ 5.4	77.4	+ 4.8
170.5	+ 1.20	25.8	+ 7.8	170.4	+ 1.2
101.2	+ 2.90	176.3	+ 1.3	101.1	+ 2.9
20.7	+ 6.20	46.6	+ 7.9	20.8	+ 6.3
201.5	+ 1.10	106.4	+ 3.3	201.4	+ 0.9
127.2	+ 1.90	207.6	+ 1.0	127.1	+ 1.9
234.3	+ 1.00	132.6	+ 2.2	38.3	+ 5.0
38.0	+ 3.80	240.6	+ 1.0	234.2	+ 0.8
155.3	+ 1.30	161.0	+ 1.6	155.2	+ 1.3
268.7	+ 0.8	275.3	+ 0.9	268.6	+ 0.8
185.4	+ 1.0	191.3	+ 1.2	185.3	+ 1.0
304.7	+ 0.7	311.6	+ 0.8	304.6	+ 0.6
49.9	- 5.4	223.5	+ 0.9	217.2	+ 0.8

Table 4.5: Refined and final holographic screen parameters.

(a) Single Turn Implementation

Diameter (mm)	Current (mA)
33 mm	3.0 mA
51.6 mm	6.5 mA
77.4 mm	12.1 mA
105.2 mm	46.4 mA

(b) Multispiral holographic screen implementation.

		ID (mm)	OD (mm)	Nt	L (μH)	Q	Current (mA)
Spiral 1	Element 1	30.8	35.2	2	14.5	96.22	1.0
	Element 2	41.9	61.3	7			
	Element 3	69.2	85.6	6			
Spiral 2	Element 4	86.6	123.8	13	29.1	126.16	4.4

Table 4.6: Single driven port holographic screen loading capacitors and excitation voltages.

	C_L(nF)	V (V)
Spiral 1	23.23	0
Spiral 2	41.55	5

4.7 References

[1] A. K. RamRakhyani, S. Mirabbasi, and M. Chiao, "Design and optimization of resonance-based efficient wireless power delivery systems for biomedical implants," *IEEE Transactions on Biomedical Circuits and Systems*, vol. 5, no. 1, pp. 48–63, Feb 2011.

[2] M. S. Chae, Z. Yang, M. R. Yuce, L. Hoang, and W. Liu, "A 128-channel 6 mw wireless neural recording ic with spike feature extraction and uwb transmitter," *IEEE Transactions on Neural Systems and Rehabilitation Engineering*, vol. 17, no. 4, pp. 312–321, Aug 2009.

[3] U. M. Jow and M. Ghovanloo, "Modeling and optimization of printed spiral coils in air, saline, and muscle tissue environments," *IEEE Transactions on Biomedical Circuits and Systems*, vol. 3, no. 5, pp. 339–347, Oct 2009.

[4] M. Kiani, U. M. Jow, and M. Ghovanloo, "Design and optimization of a 3-coil inductive link for efficient wireless power transmission," *IEEE Transactions on Biomedical Circuits and Systems*, vol. 5, no. 6, pp. 579–591, Dec 2011.

[5] P. Si, A. P. Hu, S. Malpas, and D. Budgett, "A frequency control method for regulating wireless power to implantable devices," *IEEE Transactions on Biomedical Circuits and Systems*, vol. 2, no. 1, pp. 22–29, March 2008.

[6] G. Wang, W. Liu, M. Sivaprakasam, and G. A. Kendir, "Design and analysis of an adaptive transcutaneous power telemetry for biomedical implants," *IEEE Transactions on Circuits and Systems I: Regular Papers*, vol. 52, no. 10, pp. 2109–2117, Oct 2005.

[7] Y. Mendelson, R. J. Duckworth, and G. Comtois, "A wearable reflectance pulse oximeter for remote physiological monitoring," in *2006 International Conference of the IEEE Engineering in Medicine and Biology Society*, Aug 2006, pp. 912–915.

[8] P. D. Mitcheson, "Energy harvesting for human wearable and implantable biosensors," in *2010 Annual International Conference of the IEEE Engineering in Medicine and Biology*, Aug 2010, pp. 3432–3436.

[9] W. Y. Toh, Y. K. Tan, W. S. Koh, and L. Siek, "Autonomous wearable sensor nodes with flexible energy harvesting," *IEEE Sensors Journal*, vol. 14, no. 7, pp. 2299–2306, July 2014.

[10] S. Y. Hui, "Planar wireless charging technology for portable electronic products and qi," *Proceedings of the IEEE*, vol. 101, no. 6, pp. 1290–1301, June 2013.

[11] A. P. Sample, B. H. Waters, S. T. Wisdom, and J. R. Smith, "Enabling seamless wireless power delivery in dynamic environments," *Proceedings of the IEEE*, vol. 101, no. 6, pp. 1343–1358, June 2013.

[12] E. Waffenschmidt and T. Staring, "Limitation of inductive power transfer for consumer applications," in *2009 13th European Conference on Power Electronics and Applications*, Sept 2009, pp. 1–10.

[13] W. X. Zhong, X. Liu, and S. Y. R. Hui, "A novel single-layer winding array and receiver coil structure for contactless battery charging systems with free-positioning

and localized charging features," *IEEE Transactions on Industrial Electronics*, vol. 58, no. 9, pp. 4136–4144, Sept 2011.

[14] G. A. Covic and J. T. Boys, "Inductive power transfer," *Proceedings of the IEEE*, vol. 101, no. 6, pp. 1276–1289, June 2013.

[15] G. A. Covic and J. T. Boys, "Modern trends in inductive power transfer for transportation applications," *IEEE Journal of Emerging and Selected Topics in Power Electronics*, vol. 1, no. 1, pp. 28–41, March 2013.

[16] J. Huh, S. W. Lee, W. Y. Lee, G. H. Cho, and C. T. Rim, "Narrow-width inductive power transfer system for online electrical vehicles," *IEEE Transactions on Power Electronics*, vol. 26, no. 12, pp. 3666–3679, Dec 2011.

[17] U. K. Madawala and D. J. Thrimawithana, "A bidirectional inductive power interface for electric vehicles in v2g systems," *IEEE Transactions on Industrial Electronics*, vol. 58, no. 10, pp. 4789–4796, Oct 2011.

[18] J. Shin, S. Shin, Y. Kim, S. Ahn, S. Lee, G. Jung, S. J. Jeon, and D. H. Cho, "Design and implementation of shaped magnetic-resonance-based wireless power transfer system for roadway-powered moving electric vehicles," *IEEE Transactions on Industrial Electronics*, vol. 61, no. 3, pp. 1179–1192, March 2014.

[19] D. van Wageningen and T. Staring, "The qi wireless power standard," in *Proceedings of 14th International Power Electronics and Motion Control Conference EPE-PEMC 2010*, Sept 2010, pp. S15–25–S15–32.

[20] P. McMenamin, U. M. Jow, M. Kiani, and M. Ghovanloo, "Real time control of a wireless powering and tracking system for long-term and large-area electrophysiology experiments," in *2012 IEEE Biomedical Circuits and Systems Conference (BioCAS)*, Nov 2012, pp. 240–243.

[21] E. S. Gámez Rodríguez, M. Machnoor, and G. Lazzi, "On the generation of non-diffracting beams in extremely subwavelength applications," *IEEE Transactions on Antennas and Propagation*, vol. 65, October 2017.

[22] E. Gámez, D. Schurig, and G. Lazzi, "Using signal estimation for near-field plate optimization," in *2015 IEEE International Symposium on Antennas and Propagation USNC/URSI National Radio Science Meeting*, July 2015, pp. 250–251.

[23] M. G. Abele, "Generation and confinement of uniform magnetic fields with surface currents," *IEEE Transactions on Magnetics*, vol. 41, no. 10, pp. 4179–4181, Oct 2005.

[24] A. M. Akhmeteli, A. V. Gavrilin, and W. S. Marshall, "Superconducting and resistive tilted coil magnets for generation of high and uniform transverse magnetic field," *IEEE Transactions on Applied Superconductivity*, vol. 15, no. 2, pp. 1439–1443, June 2005.

[25] J. J. Casanova, Z. N. Low, J. Lin, and R. Tseng, "Transmitting coil achieving uniform magnetic field distribution for planar wireless power transfer system," in *2009 IEEE Radio and Wireless Symposium*, Jan 2009, pp. 530–533.

[26] W.-S. Lee, H. L. Lee, K.-S. Oh, and J.-W. Yu, "Uniform magnetic field distribution of a spatially structured resonant coil for wireless power transfer," *Applied Physics Letters*, vol. 100, no. 21, p. 214105, 2012.

[27] L. Shen, W. Tang, H. Xiang, and W. Zhuang, "Uniform magnetic field of the planar coil with new winding structure for displacement-insensitive wpt," in *2014 IEEE International Conference on Communication Problem-solving*, Dec 2014, pp. 394–396.

[28] D. Yinliang, S. Yuanmao, and G. Yougang, "Design of coil structure achieving uniform magnetic field distribution for wireless charging platform," in *2011 4th International Conference on Power Electronics Systems and Applications*, June 2011, pp. 1–5.

CHAPTER 5

CONCLUSIONS

5.1 Summary of Results

The analysis and implementation of spatial filters was studied in this work. Particular emphasis was given to the potential applications of spatial filters in wireless power transfer systems. Implementation of these filters was achieved through two different methods: metamaterials and holographic screens.

Chapter 2 presents the analysis and implementation of spatial filters through metamaterials. Metamaterial research has been extremely popular during the last decades. Nonetheless, the difficulty of finding suitable unit cells limits their applications. This is particularly challenging in low frequency systems like wireless power transfer (WPT) systems, which conventionally work at or below a few MHz. At these frequencies, even extremely compact unit cells like the Swiss Roll, with a characteristic size of $\lambda_0/1000$, are too large to produce practical size metamaterial samples. In this work, we overcome this issue by proposing the use of a three-dimensional unit cell: the ferrite-loaded solenoid. It is found that the ferrite loaded solenoid provides an excellent use of its volume, and consequently, miniature sizes and high quality resonators can be fabricated from it. This unit cell was used in the fabrication of a metamaterial sample that had an overall size of 6 cm $\times$ 6 cm $\times$ 2 cm. The size and operating frequency of this metamaterial are greatly reduced when comparing the resulting design to the designs presented in similar works. The effective properties of the metamaterial sample were then extracted to validate the proposed metamaterial sample. As expected, it was found that the proposed sample resulted in negative permeability values with low loss. Finally, the metamaterial sample was used in a 2-coil WPT system in order to enhance its WPT range and efficiency. Special care was taken to guarantee that using the metamaterial would not result in a reduction of the working distance. This aspect is often overlooked in other works. To the best of our knowledge, few works have demonstrated that the metamaterial samples they

propose can minimize losses sufficiently to maintain or increase the WPT system range and working distance. The metamaterial proposed in this work achieves this together with a miniaturized size and a reduced operating frequency.

Spatial filter design through holographic screens are explored in Chapter 4. Metamaterials are easily prescribed once the desired effective properties are known. Nonetheless, the process of finding the most suitable effective properties can be very complex. Because of this, most metamaterial research is limited to applying and implementing previously known solutions. Holographic screens do not use effective properties, instead, they are prescribed through their focal plane field distribution. This difference facilitates and complicates their analysis. On one hand, prescribing a desired field transformation is easier. On the other, analyzing the properties of such a holographic screen and devising suitable implementations is complicated. In this work, harmonic decomposition is used to analyze the properties of the beam launched by a holographic screen that prescribes an arbitrary field distribution. The ability to compute the resulting field at any position in space is gained from this process, and therefore, the properties of the beam launched by the holographic screen can be analyzed and understood. Nonetheless, knowledge of the desired field distribution is not enough to prescribe a holographic screen. This issue is solved by proposing a method capable of producing a low-complexity implementation. This method is based on the orthogonal matching pursuit (OMP) algorithm. The techniques developed in this work are then used to fabricate a low-complexity holographic screen capable of launching an approximate evanescent Bessel beam. Validation is obtained through measurements of the generated field distribution and assessment of the approximate Bessel beam nondiffractive property.

Finally, the results presented in Chapter 4 are used in Chapter 5 to fabricate a lateral misalignment insensitive WPT system. Resonant inductive WPT systems rely on the inductive coupling between their receiver and transmitter coils to exchange energy. Inductive coupling decays rapidly with misalignment, and because of this, most WPT systems require careful positioning of their coils to efficiently transmit the required amount of power. Even small misalignments can result in suboptimal efficiency and insufficient or excessive power transfer, thus affecting the functioning of the receiver. It is inferred that a holographic screen that prescribes a field distribution with a uniform magnitude magnetic

field at its focal plane will result in a lateral misalignment insensitive WPT antenna. Such a holographic screen is designed using the results from Chapter 4. Nonetheless, the results of Chapter 4 are not guaranteed to result in a low-loss antenna. Because of this, transformations on the elements of the holographic screen are introduced in Chapter 5. With this transformation, reduced loss antennas are obtained at the cost of reduced field correlation. The antenna performance is then compared to the performance of a reference system extracted from the Wireless Power Consortium Qi standard. The proposed transmitter antenna delivers near constant power to a receiver at a near constant efficiency of about 85% for a range of lateral misalignment of up to 38 mm. The WPT system extracted from Qi standard does not show such a feature, since power delivery changes drastically at a fixed voltage, for any lateral misalignment.

5.2 Future Work

The current work focused on studying the properties and implementations of spatial filters, and applying these results to wireless power transfer systems. Nonetheless, controlling the field distribution and harmonic content of an exciting source is required in a wide array of applications. Microwave ablation systems, for example, are required to generate a near uniform power deposition in cancerous tissue while minimizing power deposited in surrounding healthy tissues. In principle, with spatial filters, not only can a desired treatment volume be prescribed, but this volume could also be tailored to compensate for the patient unique anatomical features through adaptive schemes. Such a holographic screen would require designing an algorithm that results in an implementation that not only excels at generating a desired field distribution, but a family of field distributions.

Likewise, magnetic stimulation is another application where control of the electromagnetic field distribution is required. Excitation voltage in these systems can be reduced increasing the gradient of the magnetic field distribution. A field distribution that can generate such a gradient with little attenuation could be devised and implemented through spatial filters.

Uniform field distribution coils are used in a variety of scientific and commercial applications. With the aid of spatial filters, it is theoretically possible to prescribe an arbitrarily uniform field distribution. Solutions that use a practically manufacturable set of elements

could be found to guarantee that the theoretical performance of the fabricated device performance.

In the area of electric vehicle wireless power transfer, uniform field distribution antennas could be utilized to transmit power to a moving car. At highway speeds, cars move too fast to deliver power efficiently when adaptive compensation systems are used. Thus, an antenna that can deliver a constant amount of power at constant efficiency is required.

Finally, the procedures developed in this work could be further refined to produce even less complex implementations that generate the prescribed field distributions with even higher accuracy. In particular, further reductions of unit cell size could be achieved if Litz wire was used instead of regular solid copper wire when metamaterial implementations are chosen. Doing this could further reduce losses and size of the resulting metamaterial sample. With regard to holographic screens, a procedure that takes into account the desired element set and designs the most suitable field distribution could be explored.